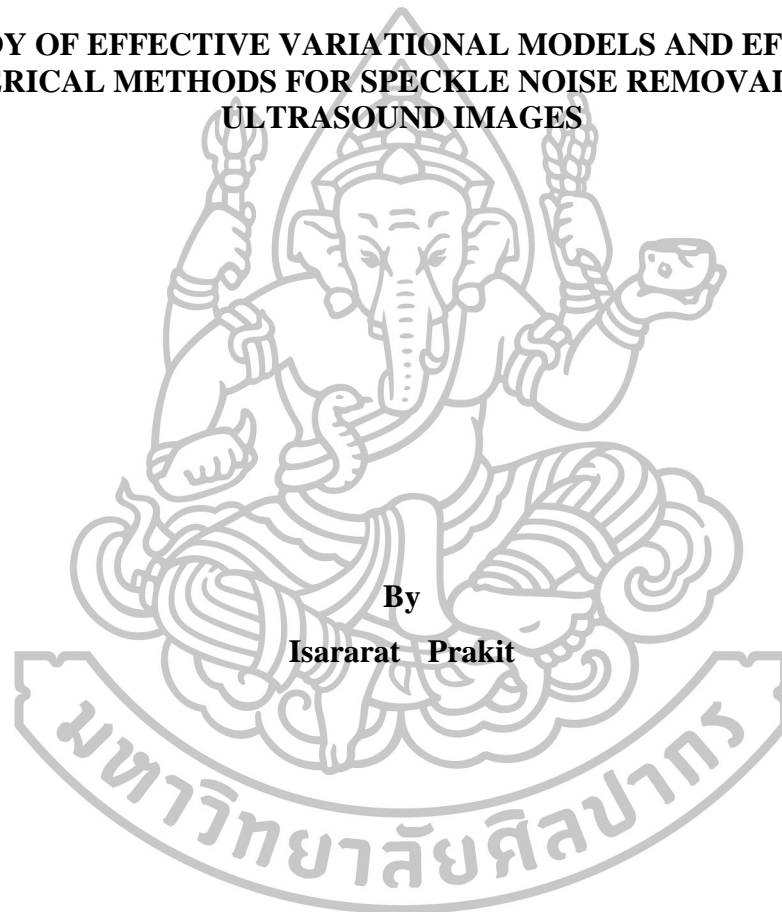




**A STUDY OF EFFECTIVE VARIATIONAL MODELS AND EFFICIENT  
NUMERICAL METHODS FOR SPECKLE NOISE REMOVAL FROM  
ULTRASOUND IMAGES**



**By  
Isararat Prakit**

**A Thesis Submitted in Partial Fulfillment of the Requirements for the Degree  
Master of Science Program in Mathematics  
Department of Mathematics  
Graduate School, Silpakorn University  
Academic Year 2015  
Copyright of Graduate School, Silpakorn University**

**A STUDY OF EFFECTIVE VARIATIONAL MODELS AND EFFICIENT  
NUMERICAL METHODS FOR SPECKLE NOISE REMOVAL FROM  
ULTRASOUND IMAGES**



**By  
Isararat Praktik**

**A Thesis Submitted in Partial Fulfillment of the Requirements for the Degree  
Master of Science Program in Mathematics  
Department of Mathematics  
Graduate School, Silpakorn University  
Academic Year 2015  
Copyright of Graduate School, Silpakorn University**

การศึกษาตัวแบบเชิงแปรผันที่มีประสิทธิผลและวิธีการเชิงตัวเลขที่มีประสิทธิภาพสำหรับกำจัด  
สัญญาณรบกวนแบบสเปกเทิลออกจากภาพคลื่นเสียงความถี่สูง



วิทยานิพนธ์นี้เป็นส่วนหนึ่งของการศึกษาตามหลักสูตรปริญญาวิทยาศาสตรมหาบัณฑิต  
สาขาวิชาคณิตศาสตร์  
ภาควิชาคณิตศาสตร์  
บัณฑิตวิทยาลัย มหาวิทยาลัยศิลปากร  
ปีการศึกษา 2558  
ลิขสิทธิ์ของบัณฑิตวิทยาลัย มหาวิทยาลัยศิลปากร

The Graduate School, Silpakorn University has approved and accredited the Thesis title of “A study of effective variational models and efficient numerical methods for speckle noise removal from ultrasound images” submitted by Miss Isararat Prakrit as a partial fulfillment of the requirements for the degree of Master of Science in Mathematics

.....  
(Associate Professor Panjai Tantatsanawong, Ph.D.)

Dean of Graduate School  
...../...../.....

The Thesis Advisor

Assistant Professor Noppadol Chumchob, Ph.D.

The Thesis Examination Committee

..... Chairman

(Associate Professor Suabsagun Yooyuanyong, Ph.D.)

...../...../.....

..... Member

(Warin Sripanya, Ph.D.)

...../...../.....

..... Member

(Assistant Professor Noppadol Chumchob, Ph.D.)

...../...../.....

56305211 : MAJOR : MATHEMATICS

KEY WORDS : IMAGE DENOISING / MULTIGRID METHOD / SPECKLE NOISE  
REMOVAL / ULTRASOUND IMAGE / VARIATIONAL MODEL

ISARARAT PRAKIT : A STUDY OF EFFECTIVE VARIATIONAL  
MODELS AND EFFICIENT NUMERICAL METHODS FOR SPECKLE NOISE  
REMOVAL FROM ULTRASOUND IMAGES. THESIS ADVISOR : ASST. PROF.  
NOPPADOL CHUMCHOB, Ph.D. 68 pp.

Ultrasound imaging technique is one of the most non-invasive, practically harmless to the human body, accurate, cost effective and real-time techniques in medical diagnosis. However, ultrasound images suffer from the so-called speckle noise because of the imaging principle. The speckle noise reduces the quality and visibility of ultrasound images, thereby decreasing overall reliability of the images and interfering with the clinical diagnosis. In this thesis, we study effective variational models and efficient numerical methods to deal with speckle noise in ultrasound images. Consequently, we first propose a novel variational model under a combination of total variation regularization and Weberized total variation regularization methods and prove the existence and uniqueness of the minimizer for the variational problem. In order to efficiently solve the associated Euler-Lagrange equation consisting of nonlinear partial differential equation, we apply a finite difference method and develop several numerical techniques for solving the resulting discrete system. Numerical experiments on various synthetic and real ultrasound images not only confirm that our improved model is effective, but also it can provide significant improvement over evaluated models. Moreover, they also show that our proposed multigrid method has great potential applications to medical ultrasound imaging technique in delivering fast, accurate, and visually pleasing restoration results.

---

Department of Mathematics

Graduate School, Silpakorn University

Student's signature .....

Academic Year 2015

Thesis Advisor's signature .....

56305211 : สาขาวิชาคณิตศาสตร์

คำสำคัญ : การกำจัดสัญญาณรบกวน / วิธีการมัลติกริด / การกำจัดสัญญาณรบกวนแบบสเปกเคิล /  
ภาพคลื่นเสียงความถี่สูง / ตัวแบบเชิงแปรผัน

อิสรารัตน์ ประกิจ : การศึกษาตัวแบบเชิงแปรผันที่มีประสิทธิผลและวิธีการเชิงตัวเลขที่มีประสิทธิภาพสำหรับกำจัดสัญญาณรบกวนแบบสเปกเคิลออกจากภาพคลื่นเสียงความถี่สูง.  
อาจารย์ที่ปรึกษาวิทยานิพนธ์ : ผศ.ดร.นพดล ชุมชอบ. 68 หน้า.

เทคนิคการสร้างภาพคลื่นเสียงความถี่สูงเป็นหนึ่งในบรรดาเทคนิคการตรวจวินิจฉัยโรคทางการแพทย์ที่ไม่ส่งผลข้างเคียงใดๆกับร่างกายของมนุษย์มีความแม่นยำสูง ประหยัดและเรียลไทม์ อย่างไรก็ตาม ภาพคลื่นเสียงความถี่สูงได้รับความเสียหายจากสัญญาณรบกวนแบบสเปกเคิลซึ่งเกิดขึ้นโดยหลักการสร้างภาพถ่ายสัญญาณรบกวนชนิดนี้ลดทอนคุณภาพและบดบังความสามารถในการมองเห็นข้อมูลที่ปรากฏในภาพซึ่งส่งผลกระทบต่อความน่าเชื่อถือของภาพและเป็นอุปสรรคในการตรวจวินิจฉัยโรคทางการแพทย์ ในวิทยานิพนธ์นี้ ผู้วิจัยศึกษาตัวแบบเชิงแปรผันที่มีประสิทธิผลและ วิธีการเชิงตัวเลขที่มีประสิทธิภาพสำหรับกำจัดสัญญาณรบกวนแบบสเปกเคิลออกจากภาพคลื่นเสียงความถี่สูง ผู้วิจัยเริ่มต้นจากการนำเสนอตัวแบบเชิงแปรผันชนิดใหม่ภายใต้การผสมวิธีการเร็กคิวลาร์ ไรซ์เซชันแบบการแปรผันรวมและ วิธีการเร็กคิวลาร์ ไรซ์เซชันแบบการแปรผันรวมอย่างเวเบอร์ จากนั้นทำการพิสูจน์การมีอยู่และการเป็นหนึ่งเดียวของผลเฉลยสำหรับปัญหาเชิงแปรผัน ในการแก้สมการออยเลอร์-ลากรางจ์ที่เกี่ยวข้องอย่างมีประสิทธิภาพ ผู้วิจัยใช้วิธีการไฟไนต์ดิฟเฟอเรนซ์และ พัฒนาวิธีการเชิงตัวเลขหลายวิธีการสำหรับแก้ระบบดิสมคริตที่เกิดขึ้น ผลการทดลองเชิงตัวเลขบนภาพสังเคราะห์และภาพคลื่นเสียงความถี่สูงจริงไม่เพียงยืนยันว่าตัวแบบเชิงแปรผันที่นำเสนอในวิทยานิพนธ์นี้มีประสิทธิผล แต่ยังคงยืนยันอีกด้วยว่าตัวแบบดังกล่าวสามารถให้ผลการกำจัดสัญญาณรบกวนที่เหนือกว่าตัวแบบอื่นๆ ที่ถูกนำมาใช้ทดสอบ ยิ่งไปกว่านั้น ผลการทดลองเชิงตัวเลขยังแสดงให้เห็นอีกด้วยว่าวิธีการมัลติกริดที่นำเสนอในวิทยานิพนธ์นี้เป็นวิธีการที่มีศักยภาพในการนำไปใช้เพื่อสร้างภาพถ่ายคลื่นเสียงความถี่สูงทางการแพทย์ที่ให้ผลการกำจัดสัญญาณรบกวนที่รวดเร็ว แม่นยำ และคมชัด

ภาควิชาคณิตศาสตร์

บัณฑิตวิทยาลัย มหาวิทยาลัยศิลปากร

ลายมือชื่อนักศึกษา.....

ปีการศึกษา 2558

ลายมือชื่ออาจารย์ที่ปรึกษาวิทยานิพนธ์ .....

## Acknowledgements

First and foremost, I wish to express my sincere and deepest appreciation to my advisor, Assistant Professor Dr. Noppadol Chumchob, for his support and guidance throughout my M.Sc. education. His broad and indepth knowledge of numerical analysis and mathematical imaging techniques guided me to explore unknown research fields. In every sense, none of this work would have been possible without him.

I would like to thank all thesis committees for their constructive criticism of my work: Associate Professor Dr. Suabsagun Yooyuanyong and Dr. Warin Sripanya.

I further would like to acknowledge with gratitude various support received from the faculty members of the Department of Mathematics at Silpakorn University during my two and a half years of M.Sc. studies. Special thanks are due to the Centre of Excellence in Mathematics (CEM) for financial support in the first year of my M.Sc. education.

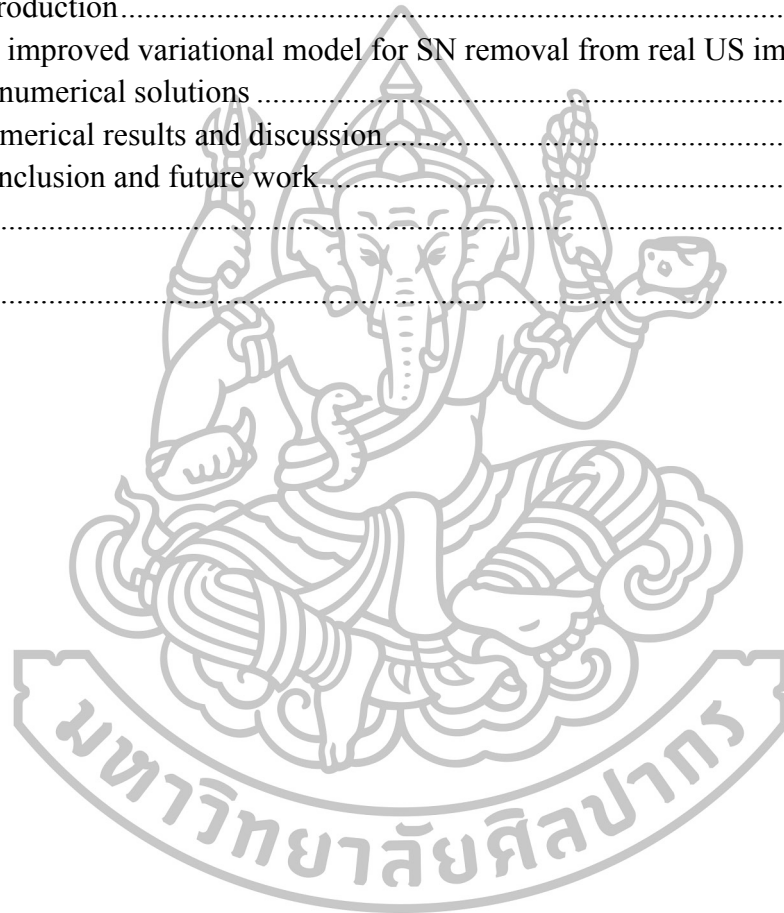
Additionally, I would like to thank my wonderful lab-mates Miss Sopida Jewprasert and Miss Satanan Thipworawimon for their helpful and insightful discussions we has along my time of M.Sc. studies.

Last, but not the least, I would like to thank my family for their unwavering support and encouragement, and their unlimited love that words cannot describe during the journey of this study.



## Table of Contents

	Page
Abstract in English.....	d
Abstract in Thai.....	e
Acknowledgments.....	f
List of Figures.....	h
List of Tables.....	j
Chapter	
1 Introduction.....	1
2 An improved variational model for SN removal from real US images and its numerical solutions.....	10
3 Numerical results and discussion.....	37
4 Conclusion and future work.....	60
References.....	61
Biography.....	68





## List of Figures

Figures	Page
3.1	The original test images. .... 38
3.2	Noisy and restored images (image: ring): ROW 1: image corrupted by SN with the standard deviation $\sigma_n^2 = 10, 15$ and 20, respectively; ROW 2: images restored using KKWV model; ROW 3: images restored using HY model; ROW 4: images restored using the proposed model ..... 40
3.3	Noisy and restored images (image: Lena): ROW 1: image corrupted by SN with the standard deviation $\sigma_n^2 = 10, 15$ and 20, respectively; ROW 2: images restored using KKWV model; ROW 3: images restored using HY model; ROW 4: images restored using the proposed model ..... 41
3.4	Noisy and restored images (image: Pepper): ROW 1: image corrupted by SN with the standard deviation $\sigma_n^2 = 10, 15$ and 20, respectively; ROW 2: images restored using KKWV model; ROW 3: images restored using HY model; ROW 4: images restored using the proposed model..... 42
3.5	Row profiles plotted for image “ring” is selected at the 128th column with 256 rows, for display at (a) $\sigma_n^2 = 10$ ; (b) $\sigma_n^2 = 15$ ; and (c) $\sigma_n^2 = 20$ ..... 45
3.6	Enlarged portions of the image Lena: (a) original image; (b) noisy image with $\sigma_n^2 = 10$ ; (c) results by KKWV model; (d) results by HY model; and (e) results by the proposed model ..... 46
3.7	Comparison with different SN removal models on a real US image of a baby. Top row (from left to right): original image; restored image by proposed model; bottom row: restored image by KKWV model; restored image by HY model. .... 47
3.8	Comparison with different SN removal models on a real US image of a human liver. Top row (from left to right): original image; restored image by proposed model; bottom row: restored image by KKWV model; restored image by model..... 48
3.9	Comparison with different SN removal models on a real US image of a human kidney. Top row (from left to right): original image; restored image by proposed model; bottom row: restored image by KKWV model; restored image by HY model..... 49
3.10	Corresponding signals of one column 128 of the baby image as shown in Fig.3.7. Top row: recovered signal by KKWV model; middle row: recovered signal by HY

	model; bottom row: recovered by the proposed model.....	50
3.11	Corresponding signals of one column 128 of the liver image as shown in Fig.3.7. Top row: recovered signal by KKWV model; middle row: recovered signal by HY model; bottom row: recovered by the proposed model .....	52
3.12	Corresponding signals of one column 128 of the kidney image as shown in Fig. 3.7. Top row: recovered signal by KKWV model; middle row: recovered signal by HY model; bottom row: recovered by the proposed model .....	53



## List of Tables

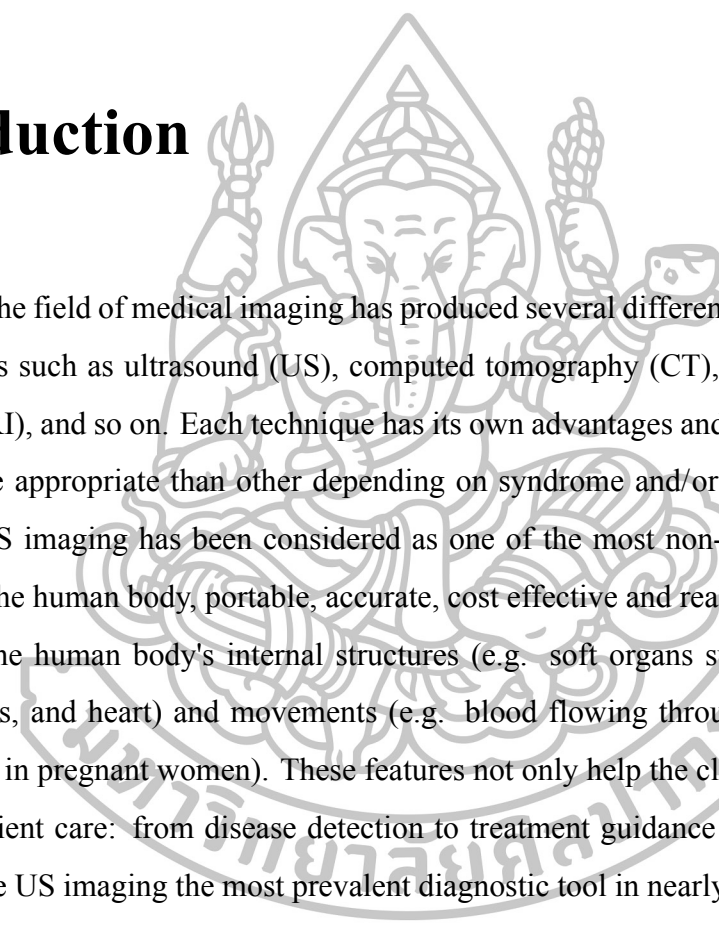
Tables		Page
3.1	SN removal models evaluated using PSNR. Test images with the size 256 x 256 corrupted by the SN generated by (1.4) with the noise standard deviation $\sigma_n^2=10$ . Recall that the last three columns show the PSNR using various SN removal models. PSNR0 means the PSNR computed from the original image $u_0$ and the initial image $u^{(0)} = z$ . Here the regularization parameters for all models were well-selected .....	43
3.2	SN removal models evaluated using ReErr. Test images with the size 256 x 256 corrupted by the SN generated by (1.4) with the noise standard deviation $\sigma_n^2=10$ . Recall that the last three columns show the PSNR using various SN removal models. PSNR0 means the PSNR computed from the original image $u_0$ and the initial image $u^{(0)} = z$ . Here the regularization parameters for all models were well-selected .....	43
3.3	Performance tests among Methods 1-5 on the three test images shown in Fig.3.1. The letters “N” and “CPUs” means the number of iterations and the total run times (in seconds). * indicates the computation was stopped after a failure in meeting Stop(1), Stop(2) or Stop(3). .....	54
3.4	Restoration results of Algorithm 4 (Proposed FAS-NMG method) with the GFP smoother for the synthetic images in Fig.3.1 corrupted by SN with the standard deviation $\sigma_n^2=10$ . Recall that $\omega = 1.2$ and $max_{SOR}=4$ were used in the GFP smoother. ....	56
3.5	Restoration results for signal-dependent tests of Algorithm 4 (Proposed FASNMG method) with the GFP smoother for the image ring shown in Fig. 3.1. Note the regularization parameters for all tests were well-selected.. ....	57
3.6	Restoration results for $\alpha_1/\alpha_2$ dependent tests of Algorithm 4 (Proposed FASNMG method) with the GFP smoother for the image ring shown in Fig. 3.1. Clearly, the small ratios between $\alpha_1$ and $\alpha_2$ , i.e. $\bar{\alpha}=0.1, 0.2, 0.5, 1$ and $2$ , are recommended. ....	58
3.7	Restoration results for $\epsilon$ -dependent tests of Algorithm 4 (Proposed FAS-NMG method) with the GFP smoother for the image ring shown in Fig. 3.1. Clearly, $\epsilon = 10^{-2}$ is	

enough to remove this kind of SN with the good PSNR results  
in a few MG steps. .... 58



# Chapter 1

## Introduction



Research in the field of medical imaging has produced several different techniques for clinical diagnosis such as ultrasound (US), computed tomography (CT), magnetic resonance imaging (MRI), and so on. Each technique has its own advantages and disadvantages. One may be more appropriate than other depending on syndrome and/or disease severity. In particular, US imaging has been considered as one of the most non-invasive, practically harmless to the human body, portable, accurate, cost effective and real-time techniques for visualizing the human body's internal structures (e.g. soft organs such as liver, kidney, spleen, uterus, and heart) and movements (e.g. blood flowing through vessels and fetal development in pregnant women). These features not only help the clinicians in almost all stages of patient care: from disease detection to treatment guidance and monitoring, but also make the US imaging the most prevalent diagnostic tool in nearly all hospitals around the world.

Basically, the US imaging is a coherent imaging system. All US images are obtained by using high-frequency sound waves, inaudible to the human ear. As the sound waves are transmitted through body tissues, they are partially reflected by the boundary between two tissue structures back to the US machine in different ways, depending on the difference in acoustic impedance of the two tissues at the interface. The time-of-flight (TOF) and the energy of the reflected echo are recorded and transformed into video or photographic images.

Note that the measurement of TOF determines the gray level of each image pixel, whereas the measurement of the echo energy provides coordinates identification of the analyzed tissues. We also note that US imaging cannot be used to create the images of bones because they are too dense to penetrate. In addition, the intestinal tract and normal lung tissue are not easily identified with this medical imaging technique because air or gas can interfere with the production of the US images.

Due to the coherent nature of the US imaging systems, the quality and visibility of the US images are limited by the noise, which originates both from physical phenomena underlying the image acquisition process and imperfections of the US imaging system. The so-called *speckle noise* (SN) is found commonly in the US images of the soft organs whose underlying structures are too small to be resolved by large wavelengths. As pointed out in [41], SN is a type of the multiplicative noise (MN), which is a random granular appearance that marks small differences in gray levels and obscures small structures. The SN occurs when there is large number of scatterers with random phase within the resolution cell of an US beam. This interfering phenomenon arises when two or more waves traveling to the probe from the scatterers interfere with each other, constructively or destructively, producing bright and dark spots. The pattern of the SN depends on the probe characteristics, such as the transducer (the US device making the sound waves and receiving the echoes) frequency and the distance from the maximum-pressure point to the transducer. In particular, the SN at high (acoustic) frequencies is less granular than at low frequencies while, its size rises as the distance of the probe source increases.

In the literature, various methods have been proposed and studied for SN reduction from US images. These methods include adaptive filtering [28, 36, 40, 41], wavelet techniques [1, 27, 37], anisotropic diffusion methods [15, 57], and variational methods [2, 30, 31, 32, 33, 34, 45, 49]. Among these SN removal techniques, the variational methods are well-established mathematical theory to offer superior image restoration quality. However, much improvement on computational complexity is a major challenge to develop fast, accurate, and stable numerical algorithms for solving associated variational problems.

In the next section, we present a mathematical framework and briefly introduce a variational formulation of US image denoising problems.

## 1.1 Mathematical framework

Let  $z : \Omega \subset \mathbb{R}^2 \rightarrow V \subset \mathbb{R}$  be an observed noisy image, where  $\Omega$  is a rectangle of  $\mathbb{R}^2$ . The goal of image denoising problems is to restore (or recover) the original image  $u : \Omega \subset \mathbb{R}^2 \rightarrow V \subset \mathbb{R}$  from the noisy image  $z$ . According to the maximum likelihood principle [24], most image denoising problems involve solving the following variational problem:

$$\min_{u \in \mathcal{U}} \{ \mathcal{J}_\alpha(u) = \mathcal{D}(u, z) + \alpha \mathcal{R}(u) \}, \quad (1.1)$$

where  $\mathcal{D}(u, z)$  is the fidelity/data term deriving from the assumption on the distribution of the noise in the observed noisy image, which is used to penalize the inconsistency between the denoised image to be restored and the observed noisy image,  $\mathcal{R}(u)$  is the regularization term, which is used to filter out the noise from the observed noisy image as well as to preserve significant features such as edges and textures of the restored image,  $\alpha > 0$  is the regularization parameter, which compromises the fidelity term  $\mathcal{D}(u, z)$  and the regularization term  $\mathcal{R}(u)$ , and  $\mathcal{U}$  is a set of admissible functions, which minimizes the energy functional  $\mathcal{J}_\alpha$ . For example, the classical model by Rudin, Osher, and Fatemi (ROF model) [44] considers the additive noise (AN) model

$$z = u + \eta \quad (1.2)$$

and minimizes the total variation (TV) regularization

$$\mathcal{R}^{\text{TV}}(u) = \int_{\Omega} |\nabla u| d\Omega$$

with the fidelity term

$$\mathcal{D}^{\text{ROF}}(u, z) = \frac{1}{2} \int_{\Omega} (u - z)^2 d\Omega.$$

Here  $\eta$  in (1.2) is the zero-mean Gaussian white noise. Note that the remarkable advantages of using the TV regularization for image denoising problems are to allow discontinuities and preserve edges in the restored images.

## 1.2 A review of variational models for SN removal

The SN model considered in many previous works is given by

$$z = u\zeta, \quad (1.3)$$

where  $\zeta$  is the MN. Unlike traditionally additive Gaussian noise model in (1.2), the noisy signals in the recorded US images are much more difficult to be removed, mainly not only because of the multiplicative nature between the noise and the original image, which is signal correlated, but also because of the noise distribution, which is generally complicated than that of Gaussian noise, commonly assumed to be Rayleigh distribution for the recorded US images.

Non-surprisingly, the choice of  $\mathcal{R}(u)$  is very crucial for restoration results. Different choices of  $\mathcal{R}(u)$  lead to different restored images. In the literature,  $\mathcal{R}^{\text{TV}}(u)$  has is commonly used as the regularization term in several variational models for SN removal, and the main difference among different variational models only comes from their image fidelity terms. As far as we know, Rudin, Lions, and Osher [45] proposed firstly the TV based variational model (RLO model) which contains a nonconvex fidelity term

$$\mathcal{D}^{\text{RLO}}(u, z) = \alpha_1 \int_{\Omega} \frac{z}{u} d\Omega + \alpha_2 \int_{\Omega} \left( \frac{z}{u} - 1 \right)^2 d\Omega$$

derived from considering  $\zeta$  to be Gaussian white noise with mean one and a very small variance, where  $\alpha_1$  and  $\alpha_2$  are the weighted parameters. This model is effective to remove the SN to a certain degree. By using the Gamma-noise assumption on  $\zeta$ , Aubert and Aujol [2] proposed a SN removal method (AA model) with the nonconvex fidelity term

$$\mathcal{D}^{\text{AA}}(u, z) = \int_{\Omega} \left( \log u + \frac{z}{u} \right) d\Omega$$

derived from the maximum a posteriori probability (MAP) estimation. Due to the nonconvexity of their fidelity terms, the corresponding algorithms may converge slowly and the computed solutions by some optimization methods are not necessary to be a global solution. To overcome these drawbacks, Shi and Osher [49] applied the logarithmic transformation



with the fidelity term in the AA model to present their convex SN removal method (SO model) and developed a nonlinear inverse scale space method for their variational technique. Afterwards, Huang et al. [30] modified differently the fidelity term in the AA model by using an exponential transformation and proposed an alternative minimization technique to solve their (strictly) convex SN removal model (HNW model). Bioucas-Dias and Figueiredo [31] applied the MAP estimation method in the logarithm domain to propose a convex SN removal method (BF model). The advantage of their BF model is that it can be efficiently solved by a fast iteration algorithm.

In clinical US imaging system, a nonlinear compression algorithm is usually applied before displaying in order to adjust the large echo dynamic range [50]. This nonlinear compression totally changes the gray level statistics of the displayed (real) US “on screen”. The authors in [4, 22, 27, 40, 50, 52] pointed out that the SN in the real US images can be modeled as corrupted with the signal-dependent MN of the form

$$z = u + \sqrt{u}\zeta, \quad (1.4)$$

where  $\zeta$  is the zero-mean Gaussian noise with the standard deviation  $\sigma_n^2$ . Based on the SN model for the real US images as represented by (1.4), the authors in [32, 34, 39] also proposed the SN removal methods including the TV regularization for SN reduction from the real US images. The authors in [39] presented a new SN removal technique (KKWV model) using the convex fidelity term

$$\mathcal{D}^{\text{KKWV}}(u, z) = \int_{\Omega} \frac{(u - z)^2}{u} d\Omega$$

resulting from (1.4) and developed an anisotropic diffusion method specially designed preserving and enhancing small vessel structures with a constrained filtering. Afterwards, a rigorous analysis of the KKWV model was discussed in [34]. The authors of this previous work first investigated into the existence and uniqueness of the minimizer for the associated variational problem and derived the existence and uniqueness of the resulting evolution equation. Recently, the authors in [32] proposed a new convex fidelity term using a gener-

alized Kullback-Leibler (KL) distance as given by

$$\mathcal{D}^{\text{HY}}(u, z) = \int_{\Omega} \left( \frac{z}{\sqrt{u}} \log \frac{z}{u} - \frac{z}{\sqrt{u}} + \sqrt{u} \right) d\Omega$$

and applied the variable splitting and Bregman iterative methods developed by [42] in the logarithm domain to efficiently solve their proposed convex SN removal model (HY model). Their numerical tests show that the HY model marginally improves over the KKWV model in terms of the restoration quality, whereas the numerical algorithm of HY model is much faster than that of KKWV model in delivering the same level of restoration quality.

### 1.3 A review of numerical techniques for SN removal

Classified by the order of its major ingredients, there are two main types of numerical schemes to compute a numerical solution of the minimization problem (1.1) for a given regularization parameter  $\alpha$ . The first is the so-called *optimize-discretize* approach and the second is the so-called *discretize-optimize* approach. The main idea of the first approach is to compute the associated Euler-Lagrange equation in the continuous domain and then solve its discretized version on the corresponding discrete domain by a method of our choices, e.g. a so-called parabolic and elliptic approach. On the other hand the latter approach aims to discretize the energy functional  $\mathcal{J}_{\alpha}$  and then solve the discrete minimization problem by standard optimization techniques, e.g. steepest descent or Newton-type methods.

#### 1.3.1 The optimize-discretize approach

For the optimize-discretize approach, the main aim is to solve the associated Euler-Lagrange (EL) equation, which generally turns out to be a nonlinear PDE

$$f(u, z) + \alpha \mathcal{A}(u) = 0 \tag{1.5}$$

subject to the appropriate boundary conditions. In other words, the approach aims to satisfy the first-order necessary condition for being a local minimizer of the energy functional

(1.1). Note that on one hand the first term  $f(u, z)$  (usually nonlinear) is related to the Gâteaux derivative of the fidelity term  $\mathcal{D}$ . On the other hand, the second term  $\mathcal{A}$  is the partial differential operator (linear or nonlinear) resulting from the Gâteaux derivative of the regularization term  $\mathcal{R}$ .

There are various numerical techniques for solving the nonlinear PDE in (1.5). These techniques can be broadly divided into two main categories: the *parabolic* and *elliptic* approaches. A parabolic approach (also known as gradient descent or time marching approach) performs by introducing the artificial time variable  $t$  and then determining the steady state solution of the time-dependent PDE:

$$\partial_t u(t) = f(u(t), z) + \alpha \mathcal{A}(u(t)), \quad (1.6)$$

where  $u(t) = u(\mathbf{x}; t)$ , typically  $u(0) = z$ . For example, if  $f$  is nonlinear and  $\mathcal{A}$  is linear, the semi-implicit scheme for (1.6) can be given by

$$\frac{u(t^{(k+1)}) - u(t^{(k)})}{\tau} = f(u(t^{(k)}), z) + \alpha \mathcal{A}(u(t^{(k+1)})) \quad (1.7)$$

where  $k \in \mathbb{N}_0$  and  $\tau > 0$  denotes the time length used to discretize  $\partial_t u(t)$ ; see [2, 31, 44, 45, 49]. For an elliptic approach it performs by directly solving the nonlinear PDE (1.5) with a method of our choice. For example, if both  $f$  and  $\mathcal{A}$  are nonlinear, the fixed-point (FP) iteration of (1.5) can be defined by

$$f(u^{[\nu]}, z) + \alpha \mathcal{A}[u^{[\nu]}](u^{[\nu+1]}) = 0 \quad (1.8)$$

where both  $f$  and  $\mathcal{A}$  are globally linearized at the current approximation  $u^{[\nu]}$  and  $\nu \in \mathbb{N}_0$  denotes the FP step; see [8, 9, 23, 47, 48].

### 1.3.2 The discretize-optimize approach

In this section, we shall briefly give the main idea of the discretize-optimize approach based in the Newton-type schemes. To this end, let us first consider the discrete minimization problem corresponding to (1.1)

$$\min_{u \in \mathcal{U}} \{ \tilde{\mathcal{J}}_\alpha(u) = \tilde{\mathcal{D}}(u, z) + \alpha \tilde{\mathcal{R}}(u) \}. \quad (1.9)$$

The next step is to linearize the discrete energy functional  $\tilde{\mathcal{J}}_\alpha$  around the current approximation  $u^{(k)}$  ( $k \in \mathbb{N}_0$ ) by the Taylor expansion given by

$$\tilde{\mathcal{J}}_\alpha(u^{(k)} + \delta u^{(k)}) = \tilde{\mathcal{J}}_\alpha(u^{(k)}) + \mathbf{J}_{\tilde{\mathcal{J}}_\alpha}^{(k)} \delta u^{(k)} + \frac{1}{2} (\delta u^{(k)})^\top \mathbf{H}_{\tilde{\mathcal{J}}_\alpha}^{(k)} \delta u^{(k)} \quad (1.10)$$

and define an (outer) iteration by

$$u^{(k+1)} = u^{(k)} + \zeta^{(k)} \delta u^{(k)}. \quad (1.11)$$

Here  $\mathbf{J}_{\tilde{\mathcal{J}}_\alpha}^{(k)}$ ,  $\mathbf{H}_{\tilde{\mathcal{J}}_\alpha}^{(k)}$  are the Jacobian and the Hessian of  $\tilde{\mathcal{J}}_\alpha$  at  $u^{(k)}$ , and  $\zeta^{(k)} > 0$  is the line-search parameter used to guarantee the reduction of  $\tilde{\mathcal{J}}_\alpha$  in each outer step  $k$ . For Newton-type methods, the perturbation  $\delta u^{(k)}$  is determined by solving the normal equation

$$\tilde{\mathbf{H}}_{\tilde{\mathcal{J}}_\alpha}^{(k)} \delta u^{(k)} = -\mathbf{J}_{\tilde{\mathcal{J}}_\alpha}^{(k)} \quad (1.12)$$

by a method of our choices (e.g. preconditioned conjugate gradient methods), considered as the inner step. Here  $\tilde{\mathbf{H}}_{\tilde{\mathcal{J}}_\alpha}^{(k)}$  is an approximate Hessian; see [54].

Although no proof exists, the first approach has an efficiency similar to that of the second one [26]. This thesis prefers the first approach. However, no matter which method is used in practical applications, both approaches are integrated with a so-called *multilevel* technique in order to provide reliable initial guesses, avoid getting in the trap of unwanted minimizers and save computational times [8, 9, 10, 11, 12, 23, 47, 48].

## 1.4 Contributions

The main aim of this thesis is to propose an improved variational model and its fast solution for the numerical approximation in removing the SN from real US images. The improved model includes the new regularization term for removing the SN. In order to efficiently solve the associated EL equation, we apply the optimize-discretize approach implemented in a nonlinear multigrid (NMG) framework as a fast and effective solver. We note that the variational model and its numerical solution to be proposed in this work are the improvement of those done in the previous works by [32, 35, 39] with several advantages. Firstly,

the proposed model is more appropriate than those in [35] for restoring real US images corrupted by the signal-dependent multiplicative noise as represented in (1.4). Secondly, the proposed model can also be considered as the generalization of the variational model in the previous work done by [39]. Next, we found what we expected in numerical experiments that our variational model provides better restoration results than those obtained from [32, 39]. Finally, as we shall demonstrate, our proposed numerical solution to be introduced in Chapter 2 is fast and efficient in providing visually pleasing SN reduction from both synthetic and real US images.

## 1.5 Summary and structure of this thesis

This thesis is composed of four chapters. Each chapter starts with its introduction, with the exception of the last chapter. Notations are introduced as the need arises. The following is the summary of the major contributions of this thesis:

- In Chapter 2, we propose the improved variational model, followed by its numerical solutions for the associated EL equation.
- In Chapter 3, experimental results from synthetic and real US images illustrating the effectiveness of the improved model and the efficiency of the proposed numerical methods are shown.
- Chapter 4 contains the conclusions of this thesis and the outlook for future research directions.

## Chapter 2

# An improved variational model for SN removal from real US images and its numerical solutions

### 2.1 Introduction

As pointed out in [35], all images are eventually perceived and interpreted by the human visual system. As a result, vision psychology and psychophysics play an essential role in the successful communication of image information. From the imaging science point of view, this fact implies that we should take into account the consequences of vision psychology and psychophysics. However, many previous works in image processing have rarely considered the influence of human vision system. In this chapter, we aim to incorporate one of the most well known and influential psychological results – Weber’s law for sound and light perception. We starting our study by proposing an improved variational model using the Weber’s law for the SN removal from real US images, followed by the study of the major mathematical properties (e.g. existence and uniqueness). Finally we present some possible methods for solving the associated EL equation.

## 2.2 The improved variational model

Weber's law was first introduced in 1834 by German physiologist Weber. The law reveals the universal influence of the background stimulus  $u$  on humans' sensitivity to the intensity increment  $\delta u$ , or the so-called JND (just-noticeable-difference), in the perception of both sound and light. The law claims that the so-called Weber's fraction is a constant:

$$\frac{\delta u}{u} = \text{cont.}$$

In this section, we apply Weber's law in the context of visual perception. Therefore,  $u$  and  $\delta u$  stand for the background light intensity and the intensity fluctuation, respectively. As mentioned in [35], our visual sensitivity to the local fluctuation  $\delta u$  depends on the ambient intensity level  $u$ . That is, variational models such as the KKWV model given by

$$\min_{u \in S(\Omega)} \{ \mathcal{J}_\alpha^{\text{KKWV}}(u) = \mathcal{D}^{\text{KKWV}}(u, z) + \alpha \mathcal{R}^{\text{TV}}(u) \}, \quad (2.1)$$

assumes that a local variation  $\delta u$  should be treated equally independent of the background intensity level  $u$ . But this exactly violates Weber's law. Note that  $S(\Omega) = \{u \in BV(\Omega), u > 0\}$  and  $BV(\Omega)$  denotes the bounded variation space, which is the space of functions  $u \in L^1(\Omega)$  such that the following quantity

$$\int_{\Omega} |Du| = \sup \left\{ \int_{\Omega} u \operatorname{div}(\varphi) d\Omega \mid \varphi \in C_0^1(\Omega; \mathbb{R}^n), |\varphi| \leq 1 \right\}$$

is finite, where  $Du$  represents the distributional gradient of  $u$ . As can be seen  $BV(\Omega)$  is a Banach space with the norm

$$\|u\|_{BV(\Omega)} = \int_{\Omega} |Du| + \|u\|_{L^1(\Omega)}.$$

Inspired from the Weberized TV (WTV) regularization method in the literature [35], we replace the new regularization term in the KKWV model as follows:

$$\mathcal{R}^{\text{TV-WTV}}(u) = \alpha_1 \int_{\Omega} |\nabla u| d\Omega + \alpha_2 \int_{\Omega} \frac{|\nabla u|}{u} d\Omega, \quad (2.2)$$

where  $\alpha_1$  and  $\alpha_2$  are the regularization parameters. Therefore, our improved KKWV model is given by

$$\min_{u \in \bar{S}(\Omega)} \{ \bar{\mathcal{J}}_{\alpha_1, \alpha_2}^{\text{KKWV}}(u) = \mathcal{D}^{\text{KKWV}}(u, z) + \mathcal{R}^{\text{TV-WTV}}(u) \}, \quad (2.3)$$

where

$$\begin{aligned} \mathcal{D}^{\text{KKWV}}(u, z) &= \int_{\Omega} \frac{(u - z)^2}{u} d\Omega, \quad h(s) = \frac{(s - z)^2}{s}, \\ \bar{S}(\Omega) &= \left\{ u \in BV(\Omega), u > 0, \int_{\Omega} \frac{|Du|}{u} < \infty \right\}, \end{aligned}$$

denotes the space of admissible functions minimizing the energy functional  $\bar{\mathcal{J}}_{\alpha}^{\text{KKWV}}$  in (2.3), resulting from the coarea formula; see [25]. As can be seen, we note first that if  $\phi(u) = \alpha_1 + \alpha_2/u$ , then (2.2) can be re-written as

$$\mathcal{R}^{\text{TV-WTV}}(u) = \int_{\Omega} \phi(u) |Du| = \alpha_1 \int_{\Omega} |Du| + \alpha_2 \int_{\Omega} \frac{|Du|}{u},$$

or

$$\mathcal{R}^{\text{TV-WTV}}(u) = \int_{\Omega} \left( \alpha_1 + \frac{\alpha_2}{u} \right) |Du|. \quad (2.4)$$

Second, when  $\alpha_2 = 0$ , our improved KKWV model (2.2) clearly reduces to the original KKWV model (2.1).

## 2.3 Mathematical analysis for the improved model

This section aims to investigate the existence and uniqueness of the minimizer to the problem (2.3).

**Theorem 2.3.1. (Existence).** *Suppose that  $z \in L^{\infty}(\Omega)$  with  $\inf_{\Omega} z > 0$ . Then the variational problem (2.3) has at least one minimizer  $\bar{u}$  in the admissible space  $\bar{S}(\Omega)$  satisfying*

$$\inf_{\Omega} z \leq \bar{u} \leq \sup_{\Omega} z.$$

*Proof.* Let us denote that  $\gamma = \inf_{\Omega} z$  and  $\beta = \sup_{\Omega} z$ . It is obvious that  $\bar{\mathcal{J}}_{\alpha_1, \alpha_2}^{\text{KKWV}}(u) \geq 0$  for all  $u \in \bar{S}(\Omega)$ . This implies that  $\bar{\mathcal{J}}_{\alpha_1, \alpha_2}^{\text{KKWV}}(u)$  has a lower bound for all  $u \in \bar{S}(\Omega)$ . Therefore, we consider a minimizing sequence  $\{u_n\} \subset \bar{S}(\Omega)$  for (2.3).



First, we show that  $\gamma \leq u_n \leq \beta$ . Since  $z \in L^\infty(\Omega)$  with  $\inf_{\Omega} z > 0$ , we can choose a sequence  $\{z_n\} \subset C^\infty(\bar{\Omega})$  such that  $z_n \rightarrow z$  in  $L^1(\Omega)$  and a.e. in  $\Omega$  as  $n \rightarrow \infty$ , and

$$\inf_{\Omega} z \leq z_n \leq \sup_{\Omega} z.$$

Replacing  $z$  in (2.3) by  $z_n$  yields  $h(s)$  is decreasing as  $s \in (0, z_n)$  and increasing as  $s \in (z_n, \infty)$  for  $n \in \mathbb{N}$ . Therefore, if  $A \geq z_n$ , we have

$$\frac{(\min(s, A) - z)^2}{\min(s, A)} \leq \frac{(s - z)^2}{s} \quad (2.5)$$

for  $\mathbf{x} \in \Omega$  and  $n \in \mathbb{N}$ . Hence, if we let  $A = \beta$ , we have

$$\int_{\Omega} \frac{(\min(u, \beta) - z_n)^2}{\min(u, \beta)} d\Omega \leq \int_{\Omega} \frac{(u - z_n)^2}{u} d\Omega.$$

Letting  $n \rightarrow \infty$  in the above inequality, using Lebesgue Convergence Theorem and (2.5), we deduce

$$\int_{\Omega} \frac{(\min(u, \beta) - z)^2}{\min(u, \beta)} d\Omega \leq \int_{\Omega} \frac{(u - z)^2}{u} d\Omega. \quad (2.6)$$

By using the results of [38] (see Lemma 1 in Sect. 4.3) and [35] (see Lemma 1 Sect. 3.2), we obtain

$$\int_{\Omega} |D(\min(u, \beta))| \leq \int_{\Omega} |Du| \quad (2.7)$$

and

$$\int_{\Omega} \frac{|D(\min(u, \beta))|}{\min(u, \beta)} \leq \int_{\Omega} \frac{|Du|}{u} \quad (2.8)$$

respectively. Combining (2.6), (2.7) and (2.8) implies that

$$\bar{\mathcal{J}}_{\alpha_1, \alpha_2}^{\text{KKWV}}(\min(u, \beta)) \leq \bar{\mathcal{J}}_{\alpha_1, \alpha_2}^{\text{KKWV}}(u).$$

On the other hand, we get in the same way that

$$\bar{\mathcal{J}}_{\alpha_1, \alpha_2}^{\text{KKWV}}(\max(u, \gamma)) \leq \bar{\mathcal{J}}_{\alpha_1, \alpha_2}^{\text{KKWV}}(u).$$

Therefore we can assume without restriction that  $\gamma \leq u_n \leq \beta$ .

Next, we prove that there exists  $u \in \bar{S}(\Omega)$  such that

$$\bar{\mathcal{J}}_{\alpha_1, \alpha_2}^{\text{KKWV}}(u) = \min_{v \in \bar{S}(\Omega)} \{ \bar{\mathcal{J}}_{\alpha_1, \alpha_2}^{\text{KKWV}}(v) \}.$$

Without loss of generality, we assume that  $\alpha_1 = \alpha_2 = 1$ . As can be seen, the above proof implies that  $u_n$  is bounded in  $L^1(\Omega)$ . Moreover, by the definition of  $\{u_n\}$ , we get that there exists a constant  $C$  such that

$$\bar{\mathcal{J}}_{\alpha_1, \alpha_2}^{\text{KKWV}}(u_n) \leq C. \quad (2.9)$$

Since  $\gamma \leq u_n \leq \beta$  and  $h \in C[\gamma, \beta]$ , we get that  $h(u_n)$  is bounded. Therefore, by using (2.9), we obtain

$$\int_{\Omega} |Du_n| \leq C.$$

Hence,  $\{u_n\}$  is bounded in  $BV(\Omega)$ . By the weak compactness,  $\{u_n\}$  has a subsequence, still denoted by  $\{u_n\}$  for simplicity, that converges strongly in  $L^1(\Omega)$  to some  $\bar{u}$ , i.e.  $u_n \rightarrow \bar{u}$ . After a refinement of the subsequence if necessary, we can assume that

$$u_n(x) \rightarrow \bar{u}(x), \text{ a.e. } \mathbf{x} \in \Omega.$$

Thus by Lebesgue's dominated convergence theorem, we obtain

$$\int_{\Omega} \frac{(\bar{u} - z)^2}{\bar{u}} d\Omega = \lim_{n \rightarrow \infty} \int_{\Omega} \frac{(u_n - z)^2}{u_n} d\Omega. \quad (2.10)$$

Applying the lower semicontinuity of the total variation term and Fatou's lemma leads to

$$\int_{\Omega} |D\bar{u}| \leq \liminf_{n \rightarrow \infty} \int_{\Omega} |Du_n|. \quad (2.11)$$

The lower semicontinuity of the Weberized total variation term can be obtained by [35] (Theorem 1 in Sect. 3.2):

$$\int_{\Omega} |D\bar{v}| \leq \liminf_{n \rightarrow \infty} \int_{\Omega} |Dv_n|, \quad (2.12)$$

where  $v_n = \log u_n$  and  $\bar{v} = \log \bar{u}$ .

Combining (2.10), (2.11), and (2.12), we have

$$\bar{\mathcal{J}}_{\alpha_1, \alpha_2}^{\text{KKWV}}(\bar{u}) \leq \liminf_{n \rightarrow \infty} \bar{\mathcal{J}}_{\alpha_1, \alpha_2}^{\text{KKWV}}(u_n).$$

It is obvious to see that  $\bar{u} \in \bar{S}(\Omega)$ . Due to  $\{u_n\}$  is the minimizing sequence, we therefore have shown that  $\bar{u}$  is in fact a minimizer of the problem (2.3).  $\square$

Unlike the several variational models discussed in Chapter 1, our improved KKWV model (2.3) is not convex due to the Weberized TV regularization term. As a result, uniqueness is no longer a direct product of convexity. To this end, we start with a computational lemma for the associated EL equation of  $\bar{\mathcal{J}}_{\alpha_1, \alpha_2}^{\text{KKWV}}(u)$ .

**Lemma 2.3.1.** *Let  $\phi(u) : (0, \infty) \rightarrow (0, \infty)$  be a  $C^1$  function and*

$$\bar{\mathcal{J}}_{\alpha_1, \alpha_2}^{\text{KKWV}}(u) = \mathcal{D}^{\text{KKWV}}(u, z) + \mathcal{R}^{\text{TV-WTV}}(u)$$

*then the formal equilibrium EL equation of  $\bar{\mathcal{J}}_{\alpha_1, \alpha_2}^{\text{KKWV}}(u)$  is given by*

$$\begin{aligned} -\phi(u) \nabla \cdot \left( \frac{\nabla u}{|\nabla u|} \right) + \left( 1 - \frac{z^2}{u^2} \right) &= 0, \\ \frac{\partial u}{\partial \mathbf{n}} \Big|_{\partial \Omega} &= 0, \end{aligned} \tag{2.13}$$

*where  $\mathbf{n}$  is the unit outward normal vector on the image boundary  $\partial \Omega$ .*

*Proof.* Applying the standard computation of Calculus of Variation

$$\bar{\mathcal{J}}_{\alpha_1, \alpha_2}^{\text{KKWV}} \rightarrow \bar{\mathcal{J}}_{\alpha_1, \alpha_2}^{\text{KKWV}} + \delta \bar{\mathcal{J}}_{\alpha_1, \alpha_2}^{\text{KKWV}}$$

leads to

$$\begin{aligned} \delta \bar{\mathcal{J}}_{\alpha_1, \alpha_2}^{\text{KKWV}} &= \int_{\Omega} \left( \phi'(u) |\nabla u| \delta u + \phi(u) \frac{\nabla u}{|\nabla u|} \cdot \nabla(\delta u) \right) d\Omega \\ &\quad + \int_{\Omega} \left( 1 - \frac{z^2}{u^2} \right) \delta u d\Omega, \\ &= \int_{\Omega} \left( \phi'(u) |\nabla u| - \nabla \cdot \left( \phi(u) \frac{\nabla u}{|\nabla u|} \right) \right) \delta u d\Omega \\ &\quad + \int_{\partial \Omega} \frac{\phi(u)}{|\nabla u|} \frac{\partial u}{\partial \mathbf{n}} \delta u dS + \int_{\Omega} \left( 1 - \frac{z^2}{u^2} \right) \delta u d\Omega, \\ &= \int_{\Omega} \left( -\phi(u) \nabla \cdot \left( \frac{\nabla u}{|\nabla u|} \right) \right) \delta u d\Omega \\ &\quad + \int_{\partial \Omega} \frac{\phi(u)}{|\nabla u|} \frac{\partial u}{\partial \mathbf{n}} \delta u dS + \int_{\Omega} \left( 1 - \frac{z^2}{u^2} \right) \delta u d\Omega, \end{aligned}$$

where  $dS$  denotes the arc-length element of the boundary.

Since  $u > 0$ , then the EL equation for  $\bar{\mathcal{J}}_{\alpha_1, \alpha_2}^{\text{KKWV}}(u)$  can be rewritten equivalently as

$$-\phi(u)\nabla \cdot \left( \frac{\nabla u}{|\nabla u|} \right) + \left( 1 - \frac{z^2}{u^2} \right) = 0,$$

$$\frac{\partial u}{\partial \mathbf{n}} \Big|_{\partial \Omega} = 0.$$

□

**Theorem 2.3.2. (Uniqueness).** Assume that  $\alpha_1 > 0$ ,  $\alpha_2 > 0$  and  $z > 0$  is in  $L^\infty(\Omega)$ , and  $u$  is a minimizer of the energy functional  $\bar{\mathcal{J}}_{\alpha_1, \alpha_2}^{\text{KKWV}}(u)$ . Then  $u$  is a unique solution in  $\bar{S}(\Omega)$ .

*Proof.* Let us denote

$$F'(u; \alpha_1, \alpha_2) = \frac{1}{\phi(u)} \left( 1 - \frac{z^2}{u^2} \right) = \frac{u^2 - z^2}{\alpha_1 u^2 + \alpha_2 u}.$$

Define a new energy function as follow:

$$\bar{\bar{\mathcal{J}}}_{\alpha_1, \alpha_2}^{\text{KKWV}}(u) = \int_{\Omega} (|\nabla u| + F(u; \alpha_1, \alpha_2)) d\Omega.$$

As can be seen, (2.13) is exactly the associated EL equation for  $\bar{\bar{\mathcal{J}}}_{\alpha_1, \alpha_2}^{\text{KKWV}}(u)$ . It is easy to find that

$$F''(u; \alpha_1, \alpha_2) = \frac{\alpha_2 u^2 + 2\alpha_1 u z^2 + \alpha_2 z^2}{(\alpha_1 u^2 + \alpha_2 u)^2}$$

is strictly convex as  $u > 0$ . Therefore, the uniqueness of the minimizer follow from the strict convexity of the energy functional  $\bar{\bar{\mathcal{J}}}_{\alpha_1, \alpha_2}^{\text{KKWV}}(u)$ . □

## 2.4 Numerical solutions of the EL equation

In this section, we introduce possible numerical solutions that could be considered for solving (2.13). To start with, the EL equation in (2.13) is rewritten as follows:

$$\underbrace{-\mathcal{K}(u) + \frac{1}{\alpha_1 u + \alpha_2} \left( u - \frac{z^2}{u} \right)}_{\mathcal{N}^h(u^h)} = g, \quad (2.14)$$

where

$$\mathcal{K}(u) = \nabla \cdot \left( \frac{\nabla u}{|\nabla u|_\epsilon} \right),$$

$$|\nabla u|_\epsilon = \sqrt{|\nabla u|^2 + \epsilon},$$

and  $0 < \epsilon \ll 1$  is a small constant to avoid division by zero. Here  $g = 0$  on the finest grid for the MG setting.

### 2.4.1 Finite difference discretization

Let  $(u^h)_{i,j} = u^h(x_{1i}, x_{2j})$  be the grid function with the uniform grid spacing  $h = 1/n$ . Here the integer  $n = 1/h$  is the number of uniform intervals in the  $x_1$  and  $x_2$  coordinate directions. Each grid point  $\mathbf{x}$  in the discretized domain  $\Omega^h$  is cell centered and given by

$$\mathbf{x} = (x_{1i}, x_{2j})^\top = ((2i-1)h/2, (2j-1)h/2)^\top$$

for  $1 \leq i, j \leq n$ . The partial derivatives in (2.14) are approximated by the standard second-order finite difference schemes. Therefore, the discrete nonlinear system is given by

$$\underbrace{-\mathcal{K}^h(u^h)_{i,j} + \alpha_\star^h(u^h)_{i,j} \left( (u^h)_{i,j} - \frac{(z^h)_{i,j}^2}{(u^h)_{i,j}} \right)}_{\mathcal{N}^h(u^h)_{i,j}} = (g^h)_{i,j}, \quad (2.15)$$

where

$$\begin{aligned} \mathcal{K}^h(u^h)_{i,j} &= -(1/h^2) \left( (\Sigma^h)_{i,j}(u^h)_{i,j} - (\bar{\Sigma}^h)_{i,j}(u^h)_{i,j} \right), \\ (\Sigma^h)_{i,j}(u^h)_{i,j} &= (D_1(u^h)_{i,j} + D_2(u^h)_{i,j} + 2D_3(u^h)_{i,j})(u^h)_{i,j}, \\ (\bar{\Sigma}^h)_{i,j}(u^h)_{i,j} &= D_1(u^h)_{i,j}(u^h)_{i-1,j} + D_2(u^h)_{i,j}(u^h)_{i,j-1} + D_3(u^h)_{i,j}(u^h)_{i+1,j} \\ &\quad + D_3(u^h)_{i,j}(u^h)_{i,j+1}, \\ D_1(u^h)_{i,j} &= D(u^h)_{i-1,j}, \\ D_2(u^h)_{i,j} &= D(u^h)_{i,j-1}, \\ D_3(u^h)_{i,j} &= D(u^h)_{i,j}, \end{aligned}$$

$$D(u^h)_{i,j} = \frac{1}{\sqrt{(\delta_x^+(u^h)_{i,j}/h)^2 + (\delta_y^+(u^h)_{i,j}/h)^2 + \epsilon}},$$

$$\delta_x^+(u^h)_{i,j} = (u^h)_{i+1,j} - (u^h)_{i,j},$$

$$\delta_y^+(u^h)_{i,j} = (u^h)_{i,j+1} - (u^h)_{i,j},$$

$$\alpha_\star^h(u^h)_{i,j} = \frac{1}{\alpha_1(u^h)_{i,j} + \alpha_2}.$$

We note that the approximations in (2.15) need to be adjusted at the image boundary  $\partial\Omega_h$  using the discrete boundary conditions

$$(u^h)_{i,1} = (u^h)_{i,2}, (u^h)_{i,n} = (u^h)_{i,n-1}, (u^h)_{1,j} = (u^h)_{2,j}, (u^h)_{n,j} = (u^h)_{n-1,j}.$$

In the following subsections the symbol ‘ $h$ ’ will sometimes drop for simplicity.

## 2.4.2 Method 1 – Semi-implicit time marching (SITM) method

As discussed in Section 1.3.1, the main idea of time marching approaches is to introduce an artificial time variable  $t$  with (2.14) and drive it to a steady state. This means that we solve

$$\frac{\partial u}{\partial t} = \mathcal{K}(u) - \alpha_\star(u) \left( u - \frac{z^2}{u} \right) \text{ for } \mathbf{x} \in \Omega \times [0, T], T > 0, \quad (2.16)$$

$$\frac{\partial u}{\partial \mathbf{n}} = 0 \text{ for } \mathbf{x} \in \partial\Omega \times [0, T], \quad (2.17)$$

$$u(0) = u_0 \text{ for } \mathbf{x} \in \Omega, \quad (2.18)$$

where  $\alpha_\star(u) = \frac{1}{\alpha_1 u + \alpha_2}$  and  $u(t) = u(\mathbf{x}; t)$ .

In order to overcome the nonlinear terms in (2.16), we may linearize (2.16) respect to the  $k + 1$ th time step using the method of ‘frozen coefficients’ as well known for variational approaches related to the TV operator (see e.g. [23, 47, 48, 54], and obtain the semi-implicit scheme as follows:

$$\frac{u(t^{(k+1)}) - u(t^{(k)})}{\tau} = \bar{\mathcal{K}}(u(t^{(k+1)})) - \alpha_\star u(t^{(k)}) \left( u(t^{(k)}) - \frac{z^2}{u(t^{(k)})} \right),$$

which we simply denote by

$$u^{(k+1)} = u^{(k)} + \tau \bar{\mathcal{K}}(u^{(k+1)}) - \tau \alpha_*(u^{(k)}) \left( u^{(k)} - \frac{z^2}{u^{(k)}} \right),$$

where  $\tau > 0$ .

Applying the finite difference discretization as discussed in Section 2.4.1 leads to

$$(u^{(k+1)})_{i,j} - \tau \bar{\mathcal{K}}(u^{(k+1)})_{i,j} = (u^{(k)})_{i,j} - \tau \alpha_*(u^{(k)})_{i,j} \times \left( (u^{(k)})_{i,j} - \frac{(z)_{i,j}^2}{(u^{(k)})_{i,j}} \right), \quad (2.19)$$

where the symbol  $h$  is dropped for simplicity,

$$\begin{aligned} \bar{\mathcal{K}}(u^{(k+1)})_{i,j} &= -(1/h^2) \left( (\Sigma^{(k)})_{i,j} (u^{(k+1)})_{i,j} - (\bar{\Sigma}^{(k)})_{i,j} (u^{(k+1)})_{i,j} \right), \\ (\Sigma^{(k)})_{i,j} (u^{(k+1)})_{i,j} &= (D_1(u^{(k)})_{i,j} + \bar{D}_2(u^{(k)})_{i,j} + 2D_3(u^{(k)})_{i,j}) (u^{(k+1)})_{i,j}, \\ (\bar{\Sigma}^{(k)})_{i,j} (u^{(k+1)})_{i,j} &= D_1(u^{(k)})_{i,j} (u^{(k+1)})_{i-1,j} + D_2(u^{(k)})_{i,j} (u^{(k+1)})_{i,j-1} \\ &\quad + D_3(u^{(k)})_{i,j} (u^{(k+1)})_{i+1,j} + D_3(u^{(k)})_{i,j} (u^{(k+1)})_{i,j+1}. \end{aligned}$$

Therefore, the update formula determined by a lexicographical ordering in a matrix-vector form can be written as

$$\mathbf{u}^{(k+1)} = \left( \mathbf{I} + \sum_{l=1}^2 \tau \mathbf{A}_{x_l}^{(k)} \right)^{-1} \mathbf{b}^{(k)}, \quad (2.20)$$

where  $\mathbf{I}$  is the identity matrix,  $\mathbf{A}_{x_l}^{(k)}$  is the coefficient matrix resulting from  $\bar{\mathcal{K}}(u^{(k+1)})_{i,j}$  along the  $x_l$  direction subject to the discrete boundary conditions, and  $\mathbf{b}^{(k)}$  is the vector determined from the right hand side of (2.19). Here

$$\begin{aligned} \mathbf{u} &= ((u)_{1,1}, (u)_{1,2}, \dots, (u)_{1,n}, (u)_{2,1}, (u)_{2,2}, \dots, (u)_{2,n}, \dots \\ &\quad (u)_{n,1}, (u)_{n,2}, \dots, (u)_{n,n})^\top \end{aligned}$$

and

$$\begin{aligned} \mathbf{b} &= ((b)_{1,1}, (b)_{1,2}, \dots, (b)_{1,n}, (b)_{2,1}, (b)_{2,2}, \dots, (b)_{2,n}, \dots \\ &\quad (b)_{n,1}, (b)_{n,2}, \dots, (b)_{n,n})^\top. \end{aligned}$$

### 2.4.3 Method 2 – Additive operator splitting (AOS) method

The second method, an additive operator splitting (AOS) method as developed by [55], is faster and more efficient than SITM method represented in (2.20). The basic idea is to replace the inverse of the sum by a sum of inverses. The corresponding iterations are then defined by

$$\mathbf{u}^{(k+1)} = \frac{1}{2} \sum_{l=1}^2 (\mathbf{I} + 2\tau \mathbf{A}_{x_l}^{(k)})^{-1} \mathbf{b}^{(k)}, \quad (2.21)$$

which is much cheaper than those obtained from (2.20) because the two tridiagonal systems in each component are solved per iteration rather than the 5-band system.

### 2.4.4 Method 3 – Fixed-point (FP) methods

As is well known, fixed point (FP) methods are successfully applied in solving the EL equations related to the TV minimization; see e.g. [3, 6, 7, 8, 9, 13, 17, 18, 19, 20, 21, 23, 29, 47, 48, 54]. This section presents three different FP methods in solving the EL equation (2.14).

#### 2.4.4.1 Global fixed-point (GFP) method

For the first FP method, the nonlinear terms  $1/|\nabla u|_c$ ,  $\alpha_*(u)$  and  $1/u$  represented in (2.14) or  $D(u)_{i,j}$ ,  $\alpha_*(u)_{i,j}$  and  $1/(u)_{i,j}$  in (2.15) may be linearized or frozen globally at a previous FP step  $\nu$ . This yields the resulting linearized system

$$\mathbf{N}[u^{[\nu]}]u^{[\nu+1]} = \mathbf{G}[u^{[\nu]}], \quad \nu = 0, 1, 2, \dots \quad (2.22)$$

where

$$\mathbf{N}[u^{[\nu]}] = -\nabla \cdot \left( \frac{\nabla}{|\nabla u^{[\nu]}|_c} \right) + \alpha_*(u^{[\nu]})\mathbf{I}$$

and

$$\mathbf{G}[u^{[\nu]}] = g + \frac{\alpha_*(u^{[\nu]})z^2}{u^{[\nu]}},$$



typically  $u^{[0]} = z$ . Classified by its ingredients, we shall name this FP method the global FP (GFP) method.

As a common way to solve (2.22) for each GFP or outer step  $\nu$ , we use the successive over-relaxation (SOR) method with the relaxation parameter  $\omega \in (0, 2)$  and then the new step at a grid point  $(x_{1_i, 2_j})$  is given by

$$(u^{[\nu+1, \bar{k}+1]})_{i,j} = (1 - \omega) (u^{[\nu+1, \bar{k}]})_{i,j} + \omega (\mathbf{N}[u^{[\nu]}])_{i,j}^{-1} (\mathbf{G}[u^{[\nu, \bar{k}+1/2]})_{i,j}, \quad (2.23)$$

where

$$(\mathbf{N}[u^{[\nu]}])_{i,j}^{-1} = \frac{1}{(1/h^2)(\Sigma^{[\nu]})_{i,j} + \alpha_*(u^{[\nu]})_{i,j}} \quad (2.24)$$

$$(\mathbf{G}[u^{[\nu, \bar{k}+1/2]})_{i,j} = (g)_{i,j} + \frac{\alpha_*(u^{[\nu]})_{i,j} (z)_{i,j}^2}{(u^{[\nu]})_{i,j}} + \frac{1}{h^2} (\bar{\Sigma}^{[\nu]})_{i,j} (u^{[\nu+1, \bar{k}+1/2]})_{i,j}, \quad (2.25)$$

and

$$\begin{aligned} (\bar{\Sigma}^{[\nu]})_{i,j} (u^{[\nu+1, \bar{k}+1/2]})_{i,j} = & D_1(u^{[\nu]})_{i,j} (u^{[\nu+1, \bar{k}+1]})_{i-1,j} \\ & + D_2(u^{[\nu]})_{i,j} (u^{[\nu+1, \bar{k}+1]})_{i,j-1} \\ & + D_3(u^{[\nu]})_{i,j} (u^{[\nu+1, \bar{k}]})_{i+1,j} \\ & + D_3(u^{[\nu]})_{i,j} (u^{[\nu+1, \bar{k}]})_{i,j+1}. \end{aligned}$$

Here the superscripts  $\bar{k}$ ,  $\bar{k} + 1/2$ , and  $\bar{k} + 1$  denote the current, intermediate and new approximations computed by the SOR method, respectively.

Obviously, for each GFP step  $\nu$  the linearized system (2.22) is strictly or irreducibly diagonally dominant. This guarantees the existence of a unique solution and global convergence of the SOR iterations [43, 46]. Moreover, the GFP method shows the interaction between the outer iteration that overcomes the nonlinearity of the discrete operator  $\mathcal{N}$  in (2.15) at each outer step  $\nu$  and the SOR method that solves the resulting linear system of equations at each corresponding inner step  $\bar{k}$ . Instead of solving the linearized system (2.22) with very high precision, the SOR method or inner iteration can perform only a *few iterations* (3 or 4) to obtain an approximate solution at each outer step  $\nu$ . This is likely

the so-called *inexact lagged-diffusivity FP* method which have been widely used for solving other problems in image processing applications related to the TV operator; see e.g. [3, 6, 7, 8, 9, 13, 17, 18, 19, 20, 21, 23, 29, 47, 48, 54]. This procedure leads to a slight difference of convergence in the GFP scheme when it is used as a stand-alone solver, whereas the computational costs significantly reduce. Moreover, the relaxation parameter  $\omega$  has a strong influence on the convergence speed. We usually use  $\omega > 1$ , typically  $\omega = 1.2$ , because it results in speeding up the convergence by many orders of magnitude faster than those of the Gauss-Seidel (GS) approach ( $\omega = 1$ ). We also note that other basic iterative techniques such as line relaxation or preconditioned conjugate gradient (PCG) method may also be used as an inner solver but they are computationally more expensive than the SOR method and therefore not recommended.

Finally, the numerical implementation to compute one iteration of the proposed GFP method (2.22) based on the SOR method (2.23) can be summarized in Algorithm 1.

#### **2.4.4.2 Local fixed-point (LFP) method**

Apart from global linearization, the alternative approach for solving the nonlinear discrete systems like (2.15) is to use methods using only *local* linearization; see e.g. [3, 6, 7, 9, 8, 21, 47, 48] and references therein. The main idea is to solve a single nonlinear equation in the given nonlinear system for a (single) unknown using a numerical method of nonlinear equations in one variable.

**Algorithm 1** (Our Proposed GFP method).

Denote by

$v$	the restored US image
$z$	the noisy US image
$g$	the RHS (right-hand side) term of (2.15)
$\alpha_1$	the regularization parameter of the TV regularization term in (2.2)
$\alpha_2$	the regularization parameter of the WTV regularization term in (2.2)
$\omega$	relaxation parameter ( $\omega = 1.2$ )
$\text{max}_{\text{SOR}}$	the maximum number of SOR iterations ( $\text{max}_{\text{SOR}} = 4$ )

---


$$[v] \leftarrow \text{GFP}(v, z, g, \alpha_1, \alpha_2, \omega, \text{max}_{\text{SOR}})$$


---

- Use input arguments to compute  $(\mathbf{N}[v])_{i,j}^{-1}$  (2.24) and the first two terms of  $(\mathbf{G}[v])_{i,j}$  in (2.25) for all  $1 \leq i, j \leq n$
  - Perform SOR steps for solving (2.22)
    - for  $k = 1 : \text{max}_{\text{SOR}}$  do
      - for  $i = 1 : n$  do
        - for  $j = 1 : n$  do
          - Compute the last term of  $(\mathbf{G}[v])_{i,j}$  in (2.25)
          - Updating  $(v^{[k+1]})_{i,j}$  using (2.23)
        - end
      - end
    - end
  - end
-

More precisely, consider the corresponding nonlinear equation for the unknowns  $(u)_{i,j-1}, (u)_{i-1,j}, (u)_{i,j}, (u)_{i+1,j}, (u)_{i,j+1}$  given by (2.15) as follows:

$$(1/h^2)((\Sigma)_{i,j}(u)_{i,j} - (\bar{\Sigma})_{i,j}(u)_{i,j}) + \alpha_\star(u)_{i,j} \left( (u)_{i,j} - \frac{(z)_{i,j}^2}{(u)_{i,j}} \right) = (g)_{i,j}.$$

Therefore, at the  $\bar{k} + 1$ th iteration a nonlinear GS step is given by

$$(1/h^2)((\Sigma^{[\bar{k}+1]})_{i,j}(u^{[\bar{k}+1]})_{i,j} - (\bar{\Sigma}^{[\bar{k}+1]})_{i,j}(u^{[\bar{k}+1]})_{i,j}) + \alpha_\star(u^{[\bar{k}+1]})_{i,j} \left( (u^{[\bar{k}+1]})_{i,j} - \frac{(z)_{i,j}^2}{(u^{[\bar{k}+1]})_{i,j}} \right) = (g)_{i,j}, \quad (2.26)$$

where

$$\begin{aligned} (\Sigma^{[\bar{k}+1]})_{i,j}(u^{[\bar{k}+1]})_{i,j} &= (D_1(u^{[\bar{k}+1]})_{i,j} + D_2(u^{[\bar{k}+1]})_{i,j} + 2D_3(u^{[\bar{k}+1]})_{i,j}) \times \\ &\quad (u^{[\bar{k}+1]})_{i,j}, \\ (\bar{\Sigma}^{[\bar{k}+1]})_{i,j}(u^{[\bar{k}+1]})_{i,j} &= D_1(u^{[\bar{k}+1]})_{i,j}(u^{[\bar{k}+1]})_{i-1,j} + D_2(u^{[\bar{k}+1]})_{i,j}(u^{[\bar{k}+1]})_{i,j-1} \\ &\quad + D_3(u^{[\bar{k}+1]})_{i,j}((u^{[\bar{k}+1]})_{i+1,j} + (u^{[\bar{k}+1]})_{i,j+1}). \end{aligned}$$

If the nonlinear terms  $D_\star(u^{[\bar{k}+1]})_{i,j}$ ,  $\alpha_\star(u^{[\bar{k}+1]})_{i,j}$  and  $1/(u^{[\bar{k}+1]})_{i,j}$  are simply replaced by  $D_\star(u^{[\bar{k}]})_{i,j}$ ,  $\alpha_\star(u^{[\bar{k}]})_{i,j}$  and  $1/(u^{[\bar{k}]})_{i,j}$ , we obtain the so-called *Gauss-Seidel-fixed point* relaxation and we shall name this numerical scheme the local FP (LFP) method. As a result, we found experimentally that this relaxation method is inefficient in leading to fast convergence. An improvement can be simply obtained by using a few more steps of FP iterations with respect to the relaxation parameter  $\omega \neq 1$  (typically  $\omega = 1.3$  and  $\max_{\text{FP}} = 2$ , where  $\max_{\text{FP}}$  denotes the maximum number of FP iterations) as follows:

$$(u^{[\bar{k}+1]})_{i,j} = (1 - \omega)(u^{[\bar{k}]})_{i,j} + \omega(\bar{u}^{[\bar{k}+1]})_{i,j}, \quad (2.27)$$

where

$$(\bar{u}^{[\bar{k}+1]})_{i,j} = \frac{(\mathbf{G}[u^{[\nu]}]_{i,j} + (1/h^2)((\bar{\Sigma}^{[\nu]})_{i,j}(u^{[\bar{k}+1/2;\nu]})_{i,j}))}{(1/h^2)(\Sigma^{[\nu]})_{i,j} + \alpha_\star(u^{[\nu]})_{i,j}}, \quad (2.28)$$

$$(\mathbf{G}[u^{[\nu]}])_{i,j} = (g)_{i,j} + \frac{\alpha_{\star}(u^{[\nu]})_{i,j}(z)_{i,j}^2}{(u)_{i,j}^{[\nu]}}, \quad (2.29)$$

$$\begin{aligned} (\bar{\Sigma}^{[\nu]})_{i,j}(u^{[\bar{k}+1/2;\nu]})_{i,j} &= D_1(u^{[\nu]})_{i,j}(u^{[\bar{k}+1]})_{i-1,j} + D_2(u^{[\nu]})_{i,j}(u^{[\bar{k}+1]})_{i,j-1} \\ &\quad + D_3(u^{[\nu]})_{i,j}((u^{[\bar{k}]})_{i+1,j} + (u^{[\bar{k}]})_{i,j+1}), \end{aligned} \quad (2.30)$$

$$(\Sigma^{[\nu]})_{i,j} = D_1(u^{[\nu]})_{i,j} + D_2(u^{[\nu]})_{i,j} + 2D_3(u^{[\nu]})_{i,j}. \quad (2.31)$$

We note that

$$D_1(u^{[\nu]})_{i,j} = \frac{1}{\sqrt{\left(\frac{(u^{[\nu]})_{i,j} - (u^{[\bar{k}+1]})_{i-1,j}}{h}\right)^2 + \left(\frac{(u^{[\bar{k}+1]})_{i-1,j+1} - (u^{[\bar{k}+1]})_{i,j-1}}{h}\right)^2 + \epsilon}},$$

$$D_2(u^{[\nu]})_{i,j} = \frac{1}{\sqrt{\left(\frac{(u^{[\bar{k}+1]})_{i+1,j-1} - (u^{[\bar{k}+1]})_{i,j-1}}{h}\right)^2 + \left(\frac{(u^{[\nu]})_{i,j} - (u^{[\bar{k}+1]})_{i,j-1}}{h}\right)^2 + \epsilon}},$$

and

$$D_3(u^{[\nu]})_{i,j} = \frac{1}{\sqrt{\left(\frac{(u^{[\bar{k}+1]})_{i+1,j} - (u^{[\nu]})_{i,j}}{h}\right)^2 + \left(\frac{(u^{[\bar{k}+1]})_{i,j+1} - (u^{[\nu]})_{i,j}}{h}\right)^2 + \epsilon}}.$$

Finally our proposed method for performing one GS iteration with  $\omega \neq 1$  (SOR iteration) can be summarized as given in Algorithm 2.

**Algorithm 2** (Our Proposed LFP method).

Denote by

- $v$  the restored US image  
 $z$  the noisy US image  
 $g$  the RHS (right-hand side) term of (2.15)  
 $\alpha_1$  the regularization parameter of the TV regularization term in (2.2)  
 $\alpha_2$  the regularization parameter of the WTV regularization term in (2.2)  
 $\omega$  relaxation parameter ( $\omega = 1.3$ )  
 $\max_{\text{FP}}$  the maximum number of inner FP iterations ( $\max_{\text{FP}} = 2$ )

---

 $[v] \leftarrow \text{LFP}(v, z, g, \alpha_1, \alpha_2, \omega, \max_{\text{FP}})$ 


---

- for  $i = 1 : n$  do  
   – for  $j = 1 : n$  do  
     – Set  $(v^{[\nu=0]})_{i,j} = (v)_{i,j}$   
     – for  $\nu = 0 : \max_{\text{FP}}$  do  
       – Compute  $(\mathbf{G}[v^{[\nu]}])_{i,j}$  using (2.29)  
       – Compute  $(\bar{\Sigma}^{[\nu]})_{i,j}(v^{[\nu]})_{i,j}$  using (2.30)  
       – Compute  $(\Sigma^{[\nu]})_{i,j}$  using (2.31)  
       – Compute  $(\bar{v})_{i,j}$  using (2.28)  
       – Set  $(v^{[\nu+1]})_{i,j} = (\bar{v})_{i,j}$   
     – end  
     – Use  $(v^{[\nu=0]})_{i,j}$ ,  $(\bar{v})_{i,j}$  and (2.27) to compute  $(v)_{i,j}$   
   – end  
 – end
-

### 2.4.4.3 Combined global-local fixed-point (CGLFP) method

The goal of this section is to show that it is possible to design a FP method that combines the advantages of GFP and LFP methods.

In the first (outer) step, we apply the GFP method. The nonlinear terms  $\alpha_*(u)_{i,j}$  and  $1/(u)_{i,j}$  in (2.15) are linearized globally at a previous FP step \*. This yields

$$(1/h^2)((\Sigma)_{i,j}(u)_{i,j} - (\bar{\Sigma})_{i,j}(u)_{i,j}) + \alpha_*(u^*)_{i,j}(u)_{i,j} = (\mathbf{G})_{i,j},$$

where

$$(\mathbf{G})_{i,j} = g_{i,j} + \frac{\alpha_*(u^*)_{i,j}(z)_{i,j}^2}{(u^*)_{i,j}}. \quad (2.32)$$

In the second (inner) step, we apply the LFP method. The resulting nonlinear system is solved by the nonlinear GS method with a few inner FP steps (2 or 3) and the relaxation parameter  $1 \neq \omega \in (0, 2)$  (typically,  $\omega = 0.9$  and  $\max_{\text{FP}} = 2$ ) as given by

$$(u^{[\bar{k}+1]})_{i,j} = (1 - \omega)(u^{[\bar{k}]})_{i,j} + \omega(\bar{u}^{[\bar{k}+1]})_{i,j}, \quad (2.33)$$

where

$$(\bar{u}^{[\bar{k}+1]})_{i,j} = \frac{1}{(1/h^2)(\Sigma^{[\nu]})_{i,j} + \alpha_*(u^*)_{i,j}} \times \left[ (\mathbf{G})_{i,j} + (1/h^2)((\bar{\Sigma}^{[\nu]})_{i,j}(u^{[\bar{k}+1/2;\nu]})_{i,j}) \right], \quad (2.34)$$

$$(\bar{\Sigma}^{[\nu]})_{i,j}(u^{[\bar{k}+1/2;\nu]})_{i,j} = D_1(u^{[\nu]})_{i,j}(u^{[\bar{k}+1]})_{i-1,j} + D_2(u^{[\nu]})_{i,j}(u^{[\bar{k}+1]})_{i,j-1} + D_3(u^{[\nu]})_{i,j}((u^{[\bar{k}]}_{i+1,j} + (u^{[\bar{k}]}_{i,j+1})), \quad (2.35)$$

$$(\Sigma^{[\nu]})_{i,j} = D_1(u^{[\nu]})_{i,j} + D_2(u^{[\nu]})_{i,j} + 2D_3(u^{[\nu]})_{i,j}, \quad (2.36)$$

$$D_1(u^{[\nu]})_{i,j} = \frac{1}{\sqrt{\left(\frac{(u^{[\nu]})_{i,j} - (u^{[\bar{k}+1]})_{i-1,j}}{h}\right)^2 + \left(\frac{(u^{[\bar{k}]}_{i-1,j+1} - (u^{[\bar{k}+1]})_{i-1,j}}{h}\right)^2} + \epsilon}},$$

$$D_2(u^{[\nu]})_{i,j} = \frac{1}{\sqrt{\left(\frac{(u^{[\bar{k}]}_{i+1,j-1} - (u^{[\bar{k}+1]})_{i,j-1}}{h}\right)^2 + \left(\frac{(u^{[\nu]})_{i,j} - (u^{[\bar{k}+1]})_{i,j-1}}{h}\right)^2} + \epsilon}},$$

$$D_3(u^{[\nu]})_{i,j} = \frac{1}{\sqrt{\left(\frac{(u^{[\bar{k}]}_{i+1,j} - (u^{[\nu]})_{i,j}}{h}\right)^2 + \left(\frac{(u^{[\bar{k}]}_{i,j+1} - (u^{[\nu]})_{i,j}}{h}\right)^2} + \epsilon}},$$

where  $\nu = 0, 1, 2, \dots$  represent the inner FP steps.  $\bar{k}$ ,  $\bar{k} + 1/2$ , and  $\bar{k} + 1$  denote respectively the current, intermediate and new approximations computed by the nonlinear GS method. We shall name this numerical scheme the combined global-local FP (CGLFP) method. Finally our proposed CGLFP method can be summarized in Algorithm 3.





**Algorithm 3** (Our Proposed CGLFP Method).

Denote by

- $v$  the restored US image  
 $z$  the noisy US image  
 $g$  the RHS (right-hand side) term of (2.15)  
 $\alpha_1$  the regularization parameter of TV regularization term in (2.2)  
 $\alpha_2$  the regularization parameter of WTV regularization term in (2.2)  
 $\omega$  relaxation parameter ( $\omega = 0.9$ )  
 $\max_{\text{FP}}$  the maximum number of inner FP iterations ( $\max_{\text{FP}} = 2$ )

$$[v] \leftarrow \text{CGLFP}(v, z, g, \alpha_1, \alpha_2, \omega, \max_{\text{FP}})$$


---

- Compute  $\alpha_*(v)_{i,j} = \frac{1}{\alpha_1(v)_{i,j} + \alpha_2}$  and  $(\mathbf{G})_{i,j}$  using (2.32) for all  $1 \leq i, j \leq n$
  - for  $i = 1 : n$  do
    - for  $j = 1 : n$  do
      - Set  $(v^{[\nu=0]})_{i,j} = (v)_{i,j}$
      - for  $\nu = 0 : \max_{\text{FP}}$  do
        - Compute  $(\bar{\Sigma}^{[\nu]})_{i,j}(v^{[\nu]})_{i,j}$  using (2.35)
        - Compute  $(\Sigma^{[\nu]})_{i,j}$  using (2.36)
        - Compute  $(\bar{v})_{i,j}$  using (2.34)
        - Set  $(v^{[\nu+1]})_{i,j} = (\bar{v})_{i,j}$
      - end
      - Use  $(v^{[\nu=0]})_{i,j}$ ,  $(\bar{v})_{i,j}$  and (2.33) to compute  $(v)_{i,j}$
    - end
  - end
-

### 2.4.5 Method 4 – Coarse-to-fine method

Common iterative solvers like the three FP methods presented in the previous sections are usually expensive and time-consuming to produce the restored US images when they are applied on a single grid. In order to gain better performance, they should involve solution on multiple grids using a so-called coarse-to-fine approach. The advantage of such an approach is that we are able to obtain a good initial solution for the fine grid problem by solving coarse grid problems. Since the coarse grid problems can be solved cheaply, it is possible to quickly find an approximate solution to the fine grid problem; using this approximate solution as an initial solution, only a few iterations are needed to provide visually pleasing restoration results on the fine grid.

Suppose that we operate with  $L$  levels in total with  $l = 1$  the coarsest level (where the image size is the smallest) and  $l = L$  the finest level (where the image size is the same as the original one). Here the size of the coarsest level 1 is chosen as  $32 \times 32$ . As a starting point, the standard coarsening is used in computing the coarse-grid domain  $\Omega^H$  by doubling the grid size in each space direction, i.e.  $h \rightarrow 2h = H$ . In order to transfer grid functions between different levels, our coarse-to-fine method uses the four-point average operator  $u_l^H = I_h^H u_l^h$  for restriction and the bi-linear interpolation operator  $u_l^h = I_H^h u_l^H$  for prolongation. Here the operators  $I_h^H$  and  $I_H^h$  are given by

$$(u_l^H)_{i,j} = \frac{1}{4}[(u_l^h)_{2i-1,2j-1} + (u_l^h)_{2i-1,2j} + (u_l^h)_{2i,2j-1} + (u_l^h)_{2i,2j}],$$

and

$$\begin{aligned} (u_l^h)_{2i,2j} &= \frac{1}{16}[9(u_l^H)_{i,j} + 3((u_l^H)_{i+1,j} + (u_l^H)_{i,j+1}) + (u_l^H)_{i+1,j+1}], \\ (u_l^h)_{2i-1,2j} &= \frac{1}{16}[9(u_l^H)_{i,j} + 3((u_l^H)_{i-1,j} + (u_l^H)_{i,j+1}) + (u_l^H)_{i-1,j+1}], \\ (u_l^h)_{2i,2j-1} &= \frac{1}{16}[9(u_l^H)_{i,j} + 3((u_l^H)_{i+1,j} + (u_l^H)_{i,j-1}) + (u_l^H)_{i+1,j-1}], \\ (u_l^h)_{2i-1,2j-1} &= \frac{1}{16}[9(u_l^H)_{i,j} + 3((u_l^H)_{i-1,j} + (u_l^H)_{i,j-1}) + (u_l^H)_{i-1,j-1}], \end{aligned}$$

respectively.

Finally, the whole procedure of Method 4 may be summarized with a recursion step as follows:

$$[u^h] \leftarrow \text{CF}(u^h, z^h, g^h, \alpha_1, \alpha_2, \omega, \max_C, \max_F)$$

- 1) If  $\Omega^h =$  coarsest grid ( $|\Omega^h| = 32 \times 32$ ), solve (2.15) using a FP method as introduced in Section 2.4.4 with  $\max_C$  steps and then stop. Else continue with following step.
- 2) Restriction to the coarse grid:  

$$u^H \leftarrow I_h^H u^h, z^H \leftarrow I_h^H z^h, g^H \leftarrow I_h^H g^h.$$
- 3) Implement the multi-resolution step on the next coarser grid:  

$$u^H \leftarrow \text{CF}(u^H, z^H, g^H, \alpha_1, \alpha_2, \omega, \max_C, \max_F).$$
- 4) Interpolation to the next finer grid:  

$$u^h \leftarrow I_H^h u^H.$$
- 5) Solve (2.15) using the FP method in 1) with  $\max_F$  steps.

#### 2.4.6 Method 5 – Full approximation scheme based nonlinear multi-grid (FAS-NMG) method

The basic idea of a MG method is to solve the problems on a series of coarse grids and interpolates coarse grid correction back to the fine grids. Performing major computational work on the coarse grids reduces significantly computation time.

One iteration of a standard MG algorithm consists of smoothing high frequency components of the error using a few steps of a smoother (an iterative relaxation technique, e.g., Jacobi, GS, and successive over relaxation (SOR) methods), solving an approximation to the smooth error equation on a coarse grid, interpolating the error correction to the fine grid, and finally adding the error correction into the current approximation (coarse-grid correction step).

An important aspect of the MG method is that the coarse grid solution can be approximated by recursively using the MG idea. That is, on the coarse grid, the smoother is performed to reduce the high frequency component of the errors followed by the projection of a residual equation on yet a coarser grid, and so on. Thus, the MG method requires a se-

ries of problems to be solved on a hierarchy of grids with different meshsizes. A multigrid V-cycle is the process that goes from the finest grid down to the coarsest grid and moves back from the coarsest up to the finest. A  $V(\nu_1; \nu_2)$ -cycle is a MG V-cycle algorithm that performs  $\nu_1$  steps of the smoother on each level before projecting the residual back to the coarse grid (pre-smoothing step), and performs  $\nu_2$  steps of the smoother after interpolating the coarse grid correction back to the fine grid (post-smoothing step). For other MG cycling algorithms and more details, we refer to [5, 51, 56].

Full approximation scheme based NMG (FAS-NMG) method has become an efficient approach for solving nonlinear problems; see e.g. [9, 10, 14, 16, 18, 19, 20, 21, 53]. Here we have to solve the nonlinear PDE (2.15), i.e.

$$\underbrace{-\mathcal{K}^h(u^h)_{i,j} + \alpha_{\star}^h(u^h)_{i,j} \left( (u^h)_{i,j} - \frac{(z^h)_{i,j}^2}{(u^h)_{i,j}} \right)}_{\mathcal{N}^h(u^h)_{i,j}} = (g^h)_{i,j}.$$

Recall that  $g^h = 0$  on the finest grid.

Let  $\bar{u}^h$  be the current approximation of  $u^h$  after a few smoothing iterations in a pre-smoothing step on a fine-grid problem where we denote by  $u^h$  the exact solution of (2.15). Then, the algebraic error  $e^h$  of the solution is given by  $e^h = u^h - \bar{u}^h$ . The nonlinear residual equation is given by

$$\mathcal{N}^h(\bar{u}^h + e^h) - \mathcal{N}^h(\bar{u}^h) = g^h - \mathcal{N}^h(\bar{u}^h) = r^h.$$

In order to correct the approximated solution  $\bar{u}^h$  on the fine grid, one needs to compute the error  $e^h$ . However, the computation of  $e^h$  is prohibitively expensive and cannot be computed directly on the fine grid. Since high frequency components of the error in the pre-smoothing step have already been removed by the smoother, we can transfer the following nonlinear system to the coarse grid as follows:

$$\underbrace{\mathcal{N}^h(\bar{u}^h + e^h)}_{\mathcal{N}^h(u^h)} = \underbrace{r^h + \mathcal{N}^h(\bar{u}^h)}_{g^h} \rightarrow \underbrace{\mathcal{N}^H(\bar{u}^H + e^H)}_{\mathcal{N}^H(u^H)} = \underbrace{r_l^H + \mathcal{N}^H(\bar{u}^H)}_{g^H} \quad (2.37)$$

where  $H = 2h$  is the new cell size  $H \times H$  and  $g^H \neq 0$  on the coarse grid. After the nonlinear residual equation on the coarse grid (2.37) has been solved with a method of our

choice, the coarse-grid correction  $e^H = u^H - \bar{u}^H$  is then interpolated back to the fine grid  $e^h$  that can now be used for updating the approximated solution  $\bar{u}^h$  of the original system on the fine grid  $\bar{u}_{new}^h = \bar{u}^h + e^h$ . The last step for a FAS-NMG method is to perform the smoother again to remove high frequency parts of the interpolated error.

The FAS-NMG components for solving (2.15) are as follows.

1. The *MG smoother* is obtained from the FP method discussed in Section 2.4.4; GFP, LFP or GLFP method.
2. The *standard coarsening method* is used in the coarse-grid domain  $\Omega^H$  by doubling the grid size in each space direction – i.e.  $h \rightarrow 2h = H$ .
3. The *intergrid transfer operators* are determined by averaging and bilinear interpolation techniques, for the restriction and interpolation operators denoted respectively by  $I_h^H$  and  $I_H^h$  as represented in the previous section.
4. The *discretization coarse grid approximation* (DCA) method is applied to compute the coarse-grid operator of  $\mathcal{N}^h(u^h)$ , where the EL system is re-discretized directly.
5. Method 1 (SITM) is used as the *coarsest grid solver* for solving the nonlinear residual equation on the coarsest grid, typically the  $4 \times 4$  grid.
6. The *MG cycle* is  $V(\nu_1; \nu_2)$ -cycle for solving the discrete nonlinear system (2.15).

For practical applications our FAS-NMG approach is stopped if the maximum number of V-cycles  $\varepsilon_1$  is reached (usually  $\varepsilon_1 = 20$ ), the relative residual obtained from the EL equation (2.15) is smaller than a small number  $\varepsilon_2 > 0$  (typically  $\varepsilon_2 = 10^{-4}$ ), the change in two consecutive steps of PSNR (see the meaning for PSNR in Chapter 3) is smaller than some  $\varepsilon_3 > 0$  (typically  $\varepsilon_3 = 10^{-2}$ ), or the change in two consecutive steps of  $J_{\alpha_1, \alpha_2}$  is smaller than a small number  $\varepsilon_4 > 0$  (typically  $\varepsilon_4 = 10^{-4}$ ). Finally, the pseudo-code implementation of our FAS-NMG method can be summarized in Algorithm 4.

We have so far presented five numerical methods for solving (2.15). So it remains to test and compare the overall performances of these numerical techniques. Their performances will be tested and reported in the next chapter.



**Algorithm 4** (FAS-NMG Algorithm).

Denote the FAS-NMG parameters as follows:

- $v^h$  the restored image
- $z^h$  the noisy image
- $g^h$  the RHS (right-hand side) term of (2.15)
- $\alpha_1$  the regularization parameter of TV regularization term in (2.2)
- $\alpha_2$  the regularization parameter of WTV regularization term in (2.2)
- $\omega$  relaxation parameter
- $\max_S$  the maximum number of iterations using by a smoother
- $\nu_1$  pre-smoothing steps on each level
- $\nu_2$  post-smoothing steps on each level
- $\vec{\varepsilon}$  the tolerance ( $\vec{\varepsilon} = (\varepsilon_1, \varepsilon_2, \varepsilon_3, \varepsilon_4)$ )

$$v^h \leftarrow \text{FASNMG} (v^h, z^h, g^h, \alpha_1, \alpha_2, \omega, \max_S, \nu_1, \nu_2, \vec{\varepsilon})$$


---

- Select and initial guess solution  $\tilde{v}_{\text{initial}}^h$  on the finest grid
  - Set  $K = 0$ ,  $(v^h)^{[K]} = \tilde{v}_{\text{initial}}^h$ ,  $\tilde{\varepsilon}_2 = \varepsilon_2 + 1$ ,  $\tilde{\varepsilon}_3 = \varepsilon_3 + 1$ , and  $\tilde{\varepsilon}_4 = \varepsilon_4 + 1$
  - While ( $K < \varepsilon_1$  AND  $\tilde{\varepsilon}_2 \geq \varepsilon_2$  AND  $\tilde{\varepsilon}_3 \geq \varepsilon_3$  AND  $\tilde{\varepsilon}_4 \geq \varepsilon_4$ )
    - ▶  $(v^h)^{[K+1]} \leftarrow \text{FASCYC}((v^h)^{[K]}, z^h, g^h, \alpha_1, \alpha_2, \omega, \max_S, \nu_1, \nu_2)$
    - ▶  $\tilde{\varepsilon}_2 = \|g^h - \mathcal{N}^h((v^h)^{[K+1]})\|_{L^2(\Omega^h)} / \|g^h - \mathcal{N}^h(\tilde{v}_{\text{initial}}^h)\|_{L^2(\Omega^h)}$
    - ▶  $\tilde{\varepsilon}_3 = |\text{PSNR}(v^h)^{[K+1]} - \text{PSNR}(v^h)^{[K]}|$ , [PSNR is given by (3.1)]
    - ▶  $\tilde{\varepsilon}_4 = |J_{\alpha_1, \alpha_2}^h((v^h)^{[K+1]}) - J_{\alpha_1, \alpha_2}^h((v^h)^{[K]})|$
    - ▶  $K = K + 1$
  - end
- 

where

$$[v^h] \leftarrow \text{FASCYC}(v^h, z^h, g^h, \alpha_1, \alpha_2, \omega, \text{max}_S, \nu_1, \nu_2)$$


---

- If  $\Omega_h = \text{coarsest grid}$  ( $|\Omega_h| = 4 \times 4$ ), solve (2.15) using (2.20) and then stop. Else continue with the following steps.

- Pre-smoothing:

$$\text{For } k = 1 \text{ to } \nu_1, [v^h] \leftarrow \text{Smoother}(v^h, z^h, g^h, \alpha_1, \alpha_2, \omega, \text{max}_S)$$

- Restriction to the coarse grid:

$$v^H \leftarrow I_h^H v^h, z^H \leftarrow I_h^H z^h$$

- Set the initial solution for the coarse-grid problem:

$$\tilde{u}^H \leftarrow v^H$$

- Compute the new right-hand side for the coarse-grid problem:

$$g^H \leftarrow I_h^H (g^h - \mathcal{N}^h(v^h)) + \mathcal{N}^H(v^H)$$

- Implement the FAS-NMG method on the coarse-grid problem:

$$[v^H] \leftarrow \text{FASCYC}(v^H, z^H, g^H, \alpha_1, \alpha_2, \omega, \text{max}_S, \nu_1, \nu_2)$$

- Add the coarse-grid corrections:

$$v^h \leftarrow v^h + I_H^h (v^H - \tilde{u}^H)$$

- Post-smoothing:

$$\text{For } k = 1 \text{ to } \nu_2, [v^h] \leftarrow \text{Smoother}(v^h, z^h, g^h, \alpha_1, \alpha_2, \omega, \text{max}_S)$$


---



# Chapter 3

## Numerical results and discussion

### 3.1 Introduction

In this chapter, we carry out numerical experiments from several test cases for both synthetic and real US images to

- (i) compare the restoration results of the proposed model in (2.2) with the state-of-the-art models for SN removal in the literature;
- (ii) illustrate the overall performances of the five numerical methods discussed in Chapter 2; and
- (iii) to assess the accuracy and efficiency of our proposed FAS-NMG technique with regard to parameter changes.

We note first that all numerical algorithms for Methods 1 – 5 were implemented in MATLAB (version R2011a) and run on a MacBook Air under OS X 10.10, at a 1.4 GHz clock speed and equipped with an Intel Core i5 and 4 GB of RAM. Second, a peak signal to noise ratio (PSNR) and a relative error (ReErr) of a restored image are used for the evaluated experiments by measuring the quality of the restored images or the ability to

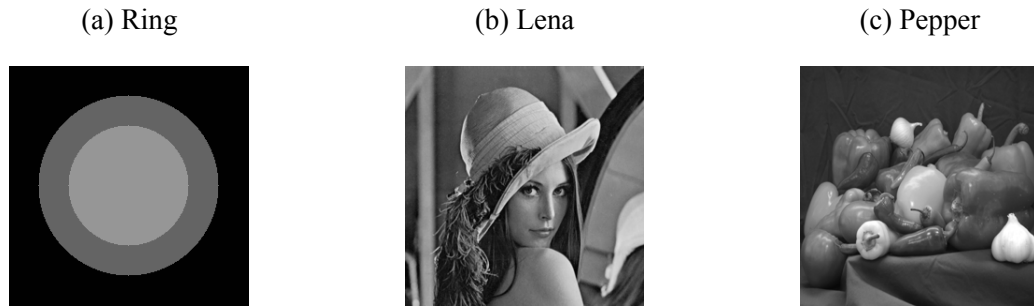


Figure 3.1: The original test images.

reduce SN from the given noisy images. The PSNR and ReErr are defined as follows:

$$\text{PSNR} = 20 \log_{10} \left[ \frac{\max_{u_0}}{\sqrt{\text{MSE}}} \right], \quad (3.1)$$

$$\text{ReErr} = \frac{\|\mathbf{u} - \mathbf{u}_0\|_2^2}{\|\mathbf{u}_0\|_2^2}, \quad (3.2)$$

where

$$\text{MSE} = \frac{1}{n^2} \sum_{i=1}^n \sum_{j=1}^n ((u)_{i,j} - (u_0)_{i,j})^2,$$

$\mathbf{u}_0$  and  $\mathbf{u}$  are respectively the vectors of  $u_0$  the original (clean) image and the restored image  $u$ . Here  $\max_{u_0}$  represents the maximum intensity value that exists in the original image.  $(u_0)_{i,j}$  and  $(u)_{i,j}$  are the sample values of the original image and the restored image at a sample point  $(x_{1_i}, x_{2_j})$ .

## 3.2 Comparison with other SN removal models

The standard test images: “ring”, “Lena” and “pepper” are used in this section to compare the performance of SN removal models in the literature and the one proposed in Chapter 2 as part of this thesis. The sizes of the three images are all the same which is  $256 \times 256$  pixels. The noise formation model in (1.4) is being assumed for creating the noisy versions

of the images. The stopping criterion of the SN removal models under consideration is that the relative difference between the successive iterates of the restored image should satisfy the following inequality:

$$\frac{\|\mathbf{u}^{[m+1]} - \mathbf{u}^{[m]}\|_2^2}{\|\mathbf{u}^{[m]}\|_2^2} < 10^{-4}. \quad (3.3)$$

We remark that there are two regularization parameters  $\alpha_1$  and  $\alpha_2$  in the proposed model. In order to reduce the computational time in the search for good regularization parameters, we fix  $\alpha_1$  in all the tests, typically  $\alpha_1 = 10^{-4}$ . Therefore, we need only determine the best value of  $\alpha_2$  for their tested values such that the relative error of the restored image  $u(\alpha_2)$  with respect to the original image  $u$  is the smallest, i.e.,

$$\frac{\|\mathbf{u}(\alpha_2) - \mathbf{u}_0\|_2^2}{\|\mathbf{u}_0\|_2^2}$$

is the smallest among all tested values of  $\alpha_2$ .

### 3.2.1 Experiments on synthetic images

Fig. 3.1 shows the original test images to be used here for the performance test in removing SN by various models.

In Fig. 3.2, we compare the performance of the proposed model with those by KKWV and HY models using the test image “ring” degraded with the standard deviation  $\sigma_n^2 = 10, 15$  and  $20$ , respectively. The first row in the figure shows the degraded images with different SN strength. The second row shows the SN removal capability of KKWV model for the noisy images shown in the first row of the figure. The third row illustrates the performance of HY model and finally the last row shows the restoration results by the proposed model under various SN noise strength. Obviously, as the SN strength increases the proposed model is significantly much better than those by other SN removal models in terms of visual appearance.

Similarly the SN removal capacity of the models considered here is further demonstrated in Figs. 3.3–3.4 for the test images “Lena” and “pepper”. The performance (in terms of SN reduction) of the proposed model is further well presented in these results.

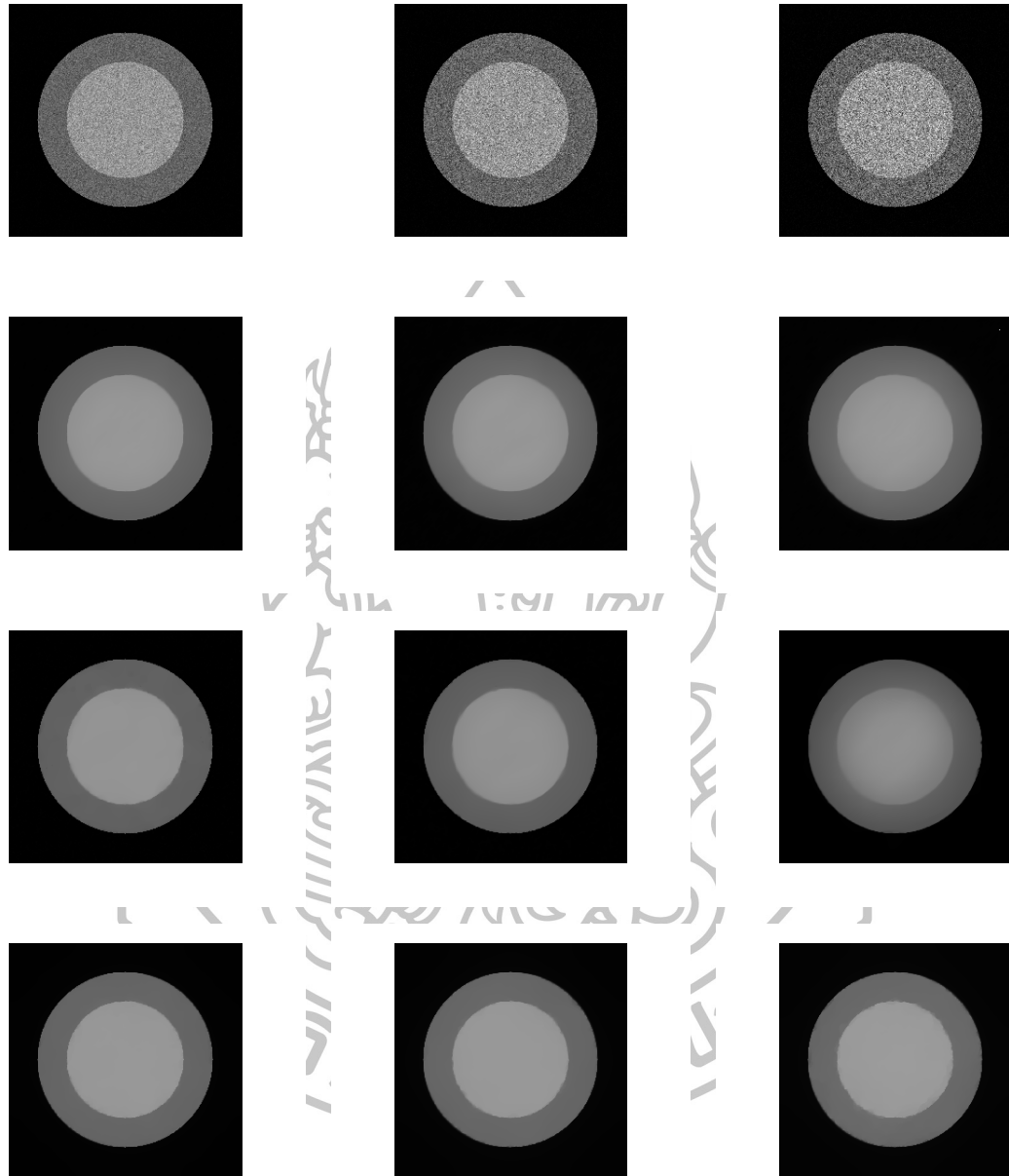


Figure 3.2: Noisy and restored images (image: ring): ROW 1: image corrupted by SN with the standard deviation  $\sigma_n^2 = 10, 15$  and  $20$ , respectively; ROW 2: images restored using KKWV model; ROW 3: images restored using HY model; ROW 4: images restored using the proposed model.



Figure 3.3: Noisy and restored images (image: Lena): ROW 1: image corrupted by SN with the standard deviation  $\sigma_n^2 = 10, 15$  and  $20$ , respectively; ROW 2: images restored using KKWV model; ROW 3: images restored using HY model; ROW 4: images restored using the proposed model.

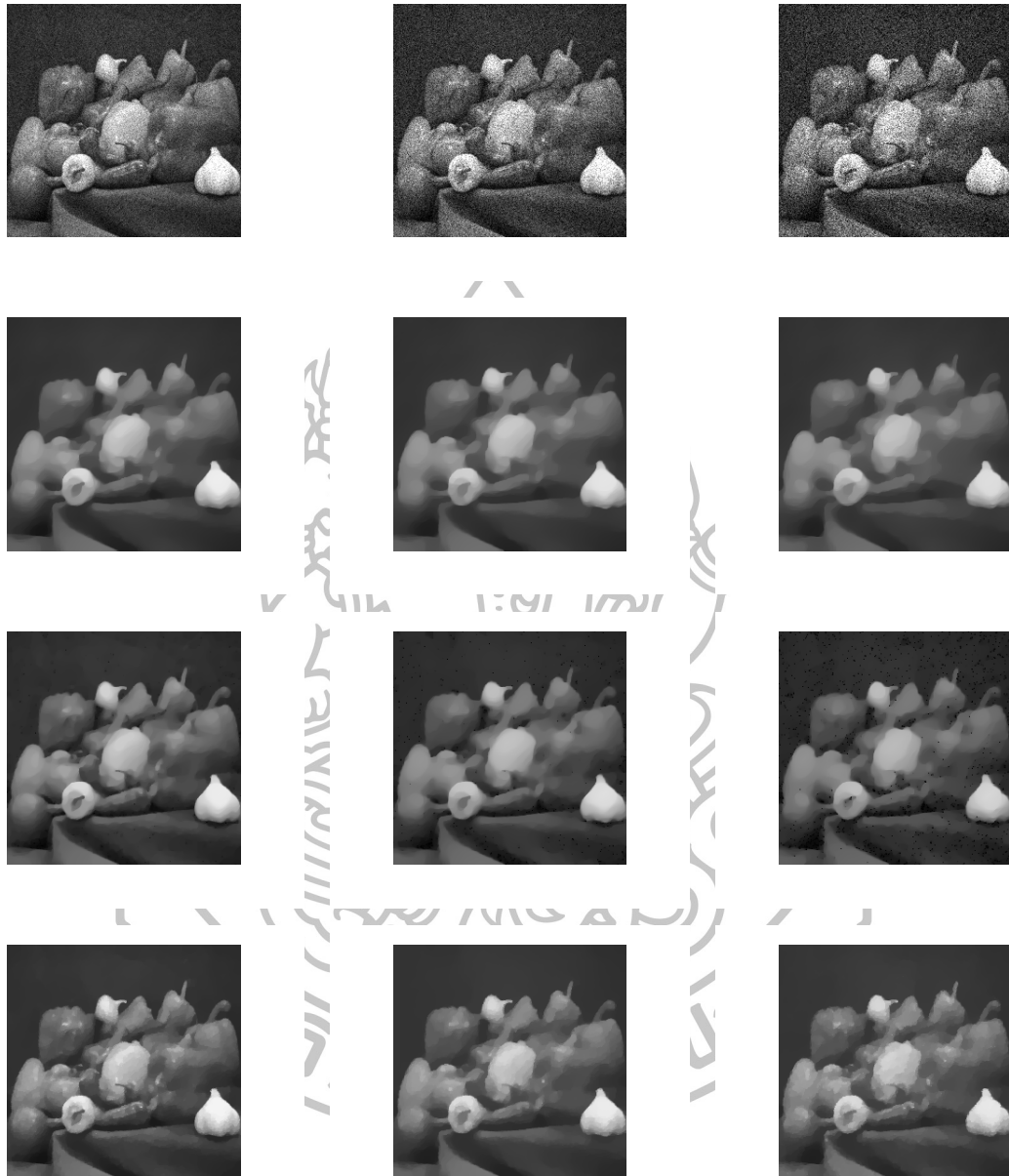


Figure 3.4: Noisy and restored images (image: pepper): ROW 1: image corrupted by SN with the standard deviation  $\sigma_n^2 = 10, 15$  and  $20$ , respectively; ROW 2: images restored using KKWV model; ROW 3: images restored using HY model; ROW 4: images restored using the proposed model.

Image	PSNR <sub>0</sub>	PSNR	PSNR	PSNR
		KKWV	HY	<b>Proposed Model</b>
Ring	25.72	37.96	38.37	<b>39.30</b>
Lena	24.10	25.50	26.10	<b>28.97</b>
Pepper	25.03	28.18	30.16	<b>32.02</b>

Table 3.1: SN removal models evaluated using PSNR. Test images with the size  $256 \times 256$  corrupted by the SN generated by (1.4) with the noise standard deviation  $\sigma_n^2 = 10$ . Recall that the last three columns show the PSNR using various SN removal models. PSNR<sub>0</sub> means the PSNR computed from the original image  $u_0$  and the initial image  $u^{(0)} = z$ . Here the regularization parameters for all models were well-selected.

Image	ReErr <sub>0</sub>	ReErr	ReErr	ReErr
		KKWV	HY	<b>Proposed Model</b>
Ring	$2.01 \times 10^{-2}$	$1.51 \times 10^{-3}$	$1.37 \times 10^{-3}$	<b><math>1.11 \times 10^{-3}</math></b>
Lena	$2.01 \times 10^{-2}$	$1.45 \times 10^{-2}$	$1.26 \times 10^{-2}$	<b><math>6.56 \times 10^{-3}</math></b>
Pepper	$2.31 \times 10^{-2}$	$1.11 \times 10^{-2}$	$7.10 \times 10^{-3}$	<b><math>4.62 \times 10^{-3}</math></b>

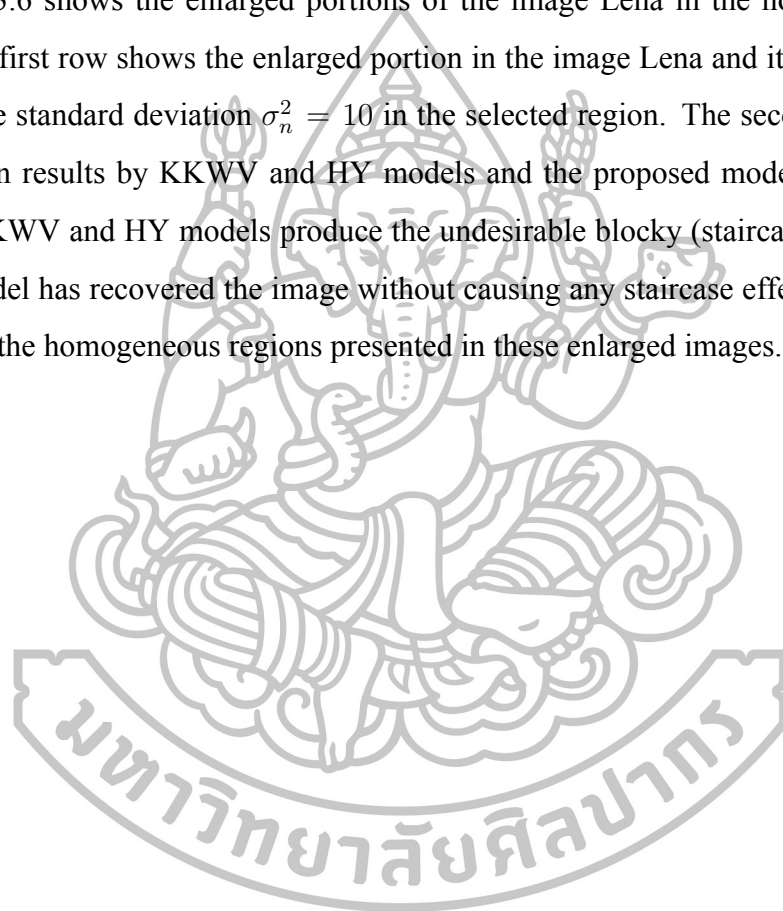
Table 3.2: SN removal models evaluated using ReErr. Test images with the size  $256 \times 256$  corrupted by the SN generated by (1.4) with the noise standard deviation  $\sigma_n^2 = 10$ . Recall that the last three columns show the ReErr using various SN removal models. ReErr<sub>0</sub> means the ReErr computed from the original image  $u_0$  and the initial image  $u^{(0)} = z$ . Here the regularization parameters for all models were well-selected.

Tab. 3.1 and Tab. 3.2 show respectively the PSNR and ReErr of the restored images produced by the proposed model and other SN removal models for different test images. In this experiment, the test images are corrupted by a SN with the noise standard deviation  $\sigma_n^2 = 10$ . As expected, it is clear that the PSNR and ReErr of the restored images are much better for the proposed model compared with those of other models considered here.

Fig. 3.5 shows a one-dimensional profile of the image: “ring” (128th column with

256 rows) treated with other models and the proposed one. The original, noisy and restored images are shown in the figure with the noise standard deviation  $\sigma_n^2 = 10, 15$  and  $20$ . It can be observed from Fig. 3.5 that all models can be used to remove SN from the noisy images. However, as the SN strength increases the proposed model yields better restoration quality for reducing SN.

Fig. 3.6 shows the enlarged portions of the image Lena in the homogeneous of regions. The first row shows the enlarged portion in the image Lena and its noisy version with the noise standard deviation  $\sigma_n^2 = 10$  in the selected region. The second row shows the restoration results by KKWV and HY models and the proposed model. We can see that while KKWV and HY models produce the undesirable blocky (staircase) images, the proposed model has recovered the image without causing any staircase effect. This fact is evident from the homogeneous regions presented in these enlarged images.





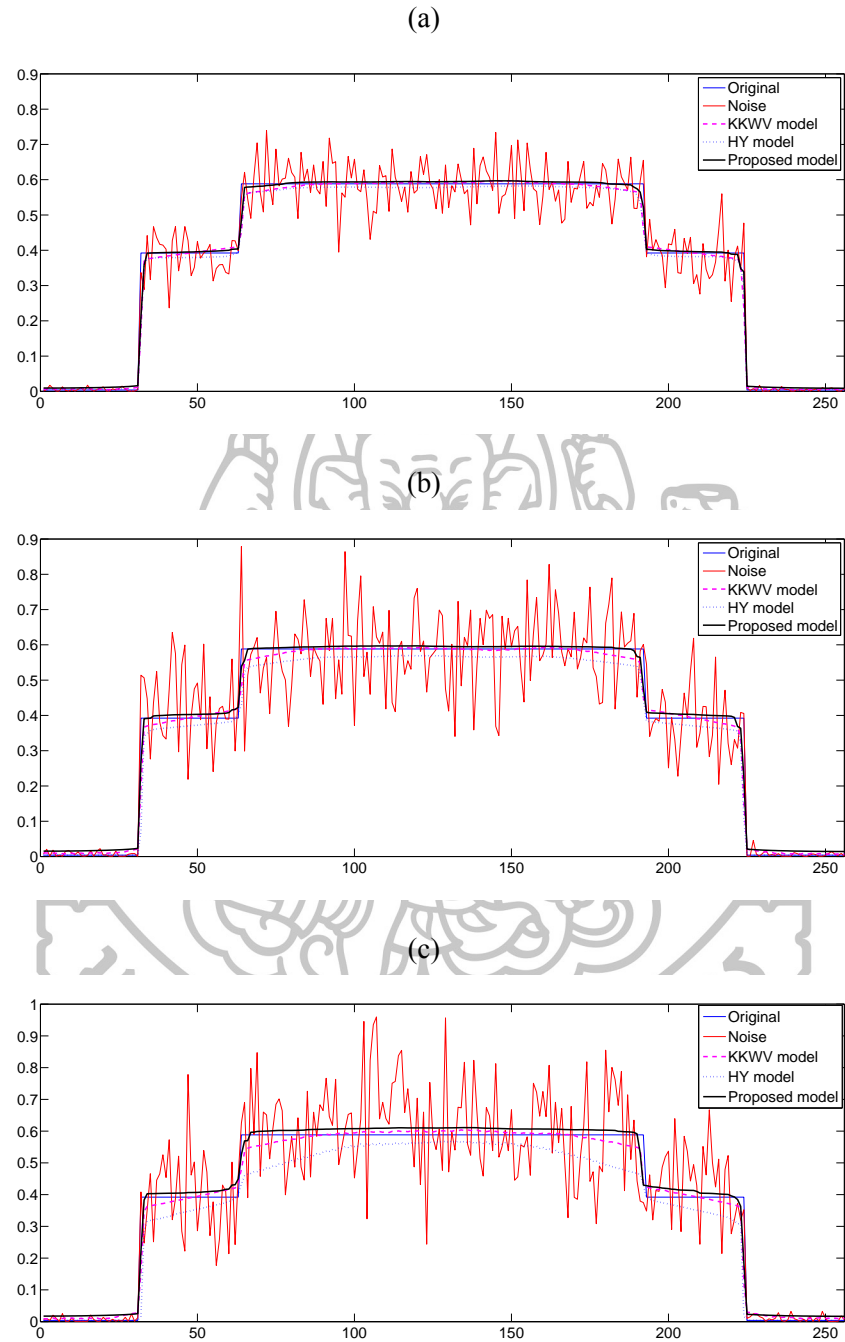


Figure 3.5: Row profiles plotted for image “ring” is selected at the 128th column with 256 rows, for display at (a)  $\sigma_n^2 = 10$ ; (b)  $\sigma_n^2 = 15$ ; and (c)  $\sigma_n^2 = 20$ .

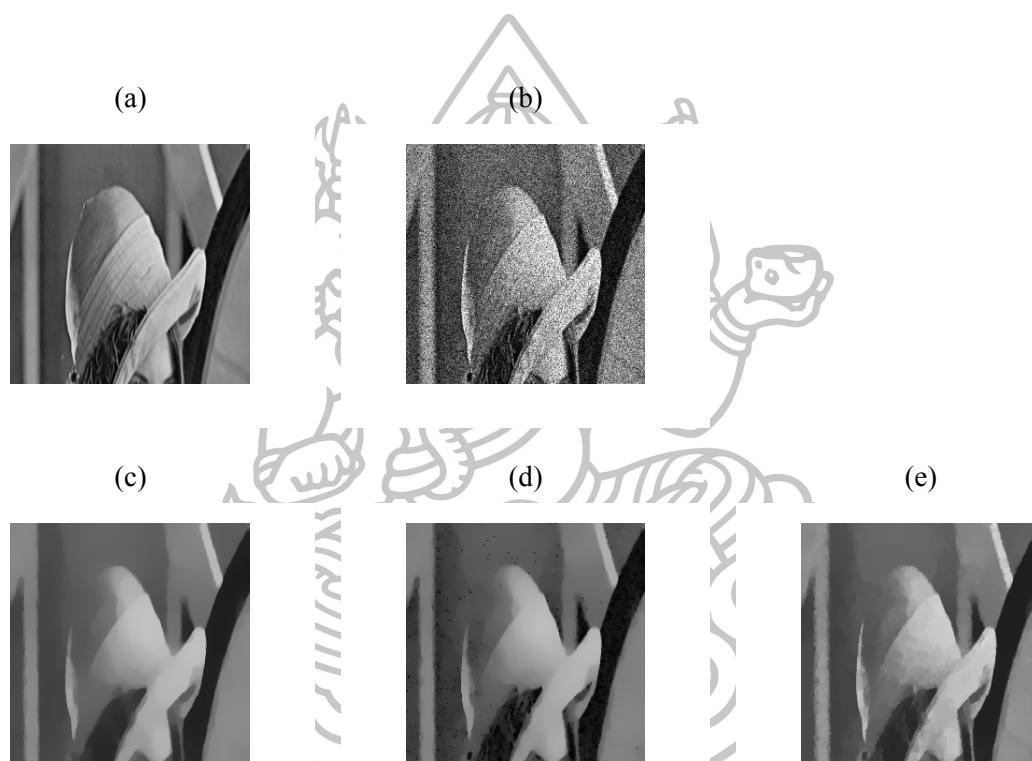


Figure 3.6: Enlarged portions of the image Lena: (a) original image; (b) noisy image with  $\sigma_n^2 = 10$ ; (c) results by KKWV model; (d) results by HY model; and (e) results by the proposed model.

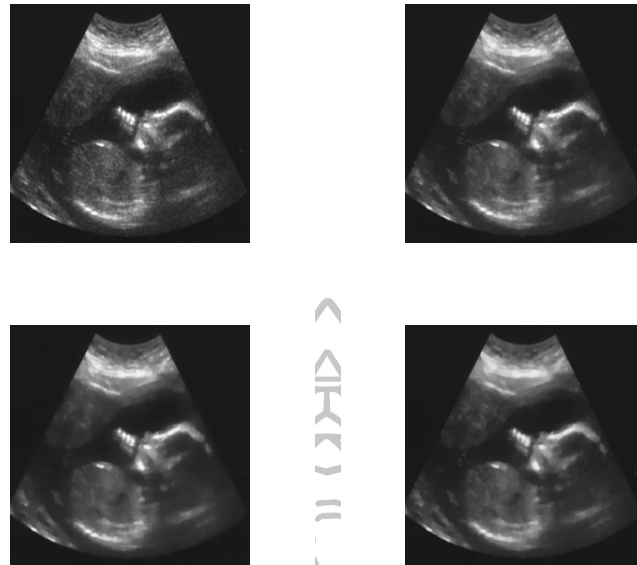


Figure 3.7: Comparison with different SN removal models on a real US image of a baby. Top row (from left to right): original image; restored image by proposed model; bottom row: restored image by KKWV model; restored image by HY model.

### 3.2.2 Experiments on real US images

In this part, we test the performance of the proposed model and compared with other two models using three real US images, “baby”, “liver” and “kidney”. These real US images from different medical applications are the same size which is  $256 \times 256$  pixels and corrupted with unknown SN strength.

The first rows in Figs. 3.7–3.9 show the real US images and the restored images by the proposed model. The last rows in Figs. 3.7–3.9 show the restored images by KKWV and HY models.

Figs. 3.10–3.12 (from top-to-bottom) show the corresponding signal of one column 128 and the restored signal by KKWV model, HY model and the proposed model. As is evident from Figs. 3.7–3.9, the proposed model restores the real US images with a better visual quality reduced amount of SN in comparison with the other models. Moreover, Figs.

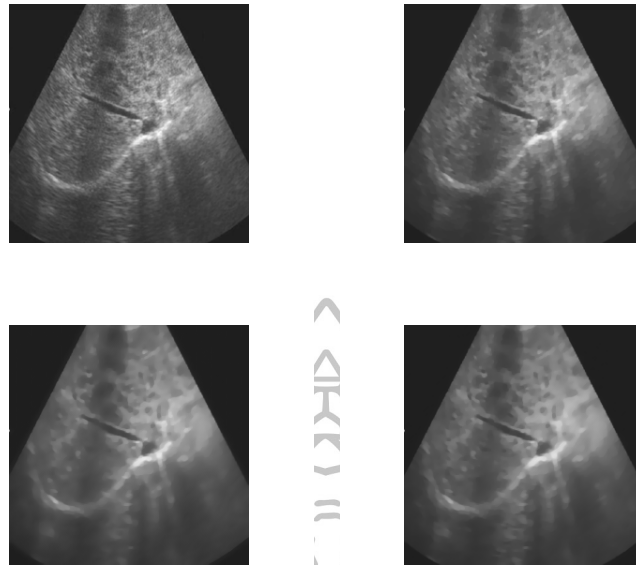


Figure 3.8: Comparison with different SN removal models on a real US image of a human liver. Top row (from left to right): original image; restored image by proposed model; bottom row: restored image by KKWV model; restored image by HY model.

3.10–3.12 indicate that the staircase effects are observable in the restored images produced by KKWV and HY model, whereas the staircase effect is not so evident in the images resulting from our proposed model.

### 3.3 Performance tests among Methods 1–5

To illustrate the performance of Methods 1–5, the three test images with the  $256 \times 256$  pixels as shown in Fig. 3.1 are used here and distorted by a SN with  $\sigma_n^2 = 10$ . All methods starts with the same initial solution  $u^{[0]} = z$ . In this section we will use following common stopping rules:

- 1)  $\text{Stop}(1) = \|g - \mathcal{N}(u^{(\text{new})})\|_{L^2(\Omega)} / \|g - \mathcal{N}(u^{[0]})\|_{L^2(\Omega)} < 10^{-4}$ .
- 2)  $\text{Stop}(2) = |\text{PSNR}(u^{(\text{new})}) - \text{PSNR}(u^{(\text{old})})| < 10^{-6}$ .

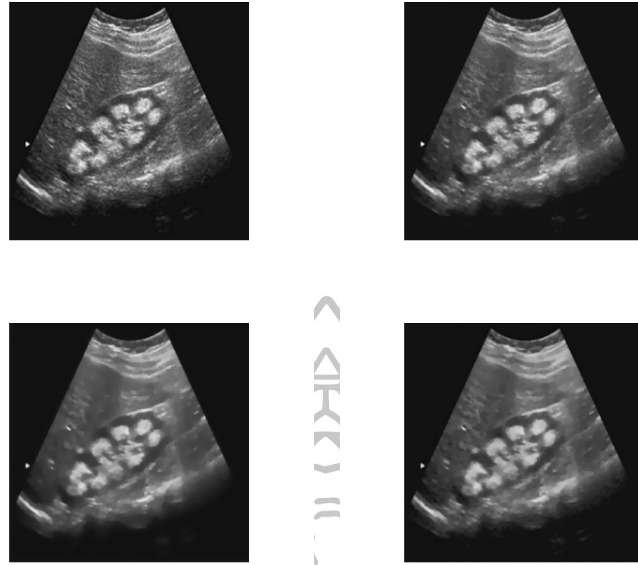


Figure 3.9: Comparison with different SN removal models on a real US image of a human kidney. Top row (from left to right): original image; restored image by proposed model; bottom row: restored image by KKWV model; restored image by HY model.

$$3) \text{ Stop}(3) = |J_{\alpha_1, \alpha_2}(u^{(\text{new})}) - J_{\alpha_1, \alpha_2}(u^{(\text{old})})| < 10^{-6}.$$

$$4) \text{ Stop}(4) = (\text{iter} \geq 1000).$$

Recall that  $u^{(\text{new})}$  and  $u^{(\text{old})}$  represent the restored images from the current and previous iterations and “iter” denotes for the number of iterations used by Methods 1–5.

For Methods 1–2, the parameter  $\tau$  needs to be given to start up our time marching algorithms. Although we may obtain better restoration results for very small values of  $\tau$ , the algorithms will be time-consuming. In contrast, if it is set to be very large, the algorithms will not converge. In this section, we found experimentally from several cases that setting  $\tau = 5 \times 10^{-5}$  is an appropriate choice which can make a good balance between the run times and the SN removal performance. For Method 3, we also found experimentally that the FP parameters,  $(\omega, \max_{\text{SOR}}) = (1.2, 4)$ ,  $(\omega, \max_{\text{FP}}) = (1.3, 2)$  and  $(\omega, \max_{\text{SOR}}) = (0.9, 2)$ , are optimal in leading to fast convergence and visually pleasing restoration results for GFP,

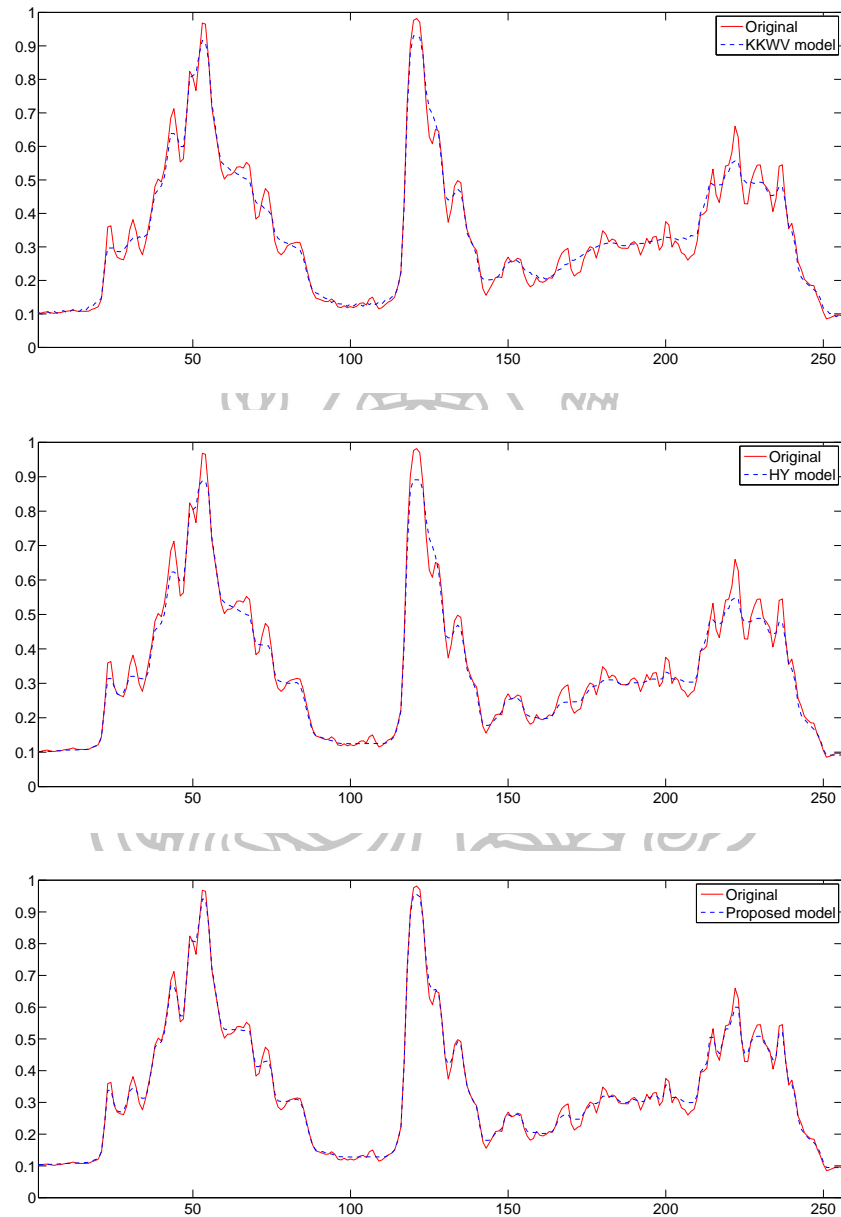
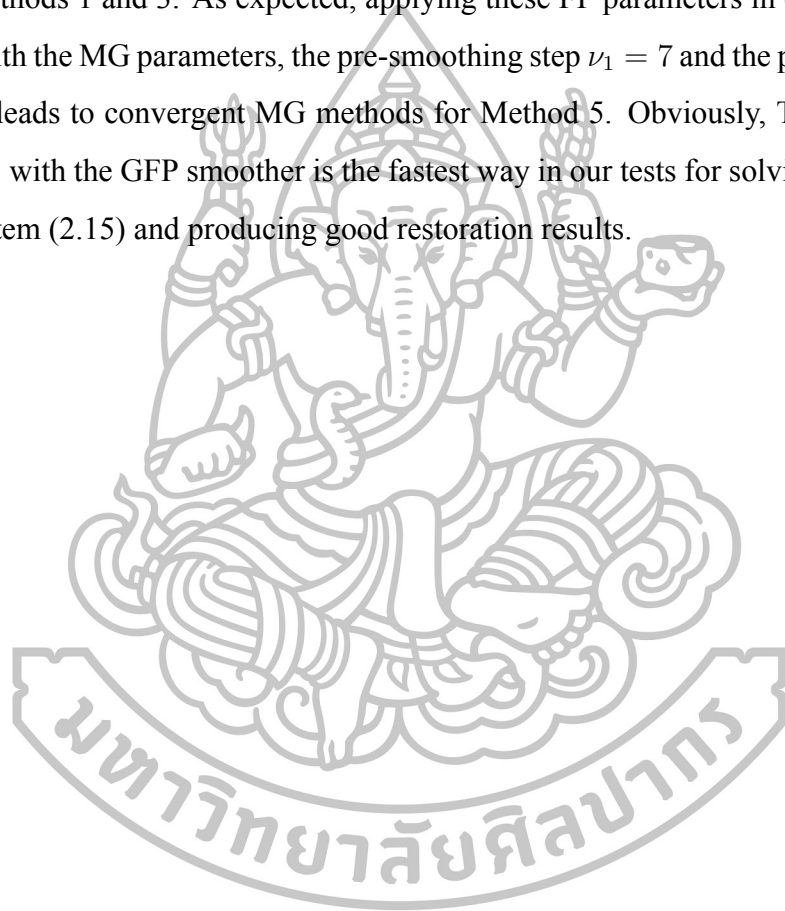


Figure 3.10: Corresponding signals of one column 128 of the baby image as shown in Fig. 3.7. Top row: recovered signal by KKWV model; middle row: recovered signal by HY model; bottom row: recovered by the proposed model.

LFP and CGLFP methods, respectively. As can be seen, Method 3 is more efficient than Methods 1 and 2. Further, we had applied these sets of parameters with Methods 4 and 5. We found first that restoring by Method 4 with  $\max_c = 1000$  and  $\max_F = 100$  outperforms other choices of these parameters in terms of visual appearance and computation time for SN removal performance. However, Method 4 is better than Method 2, but it is less efficient than Methods 1 and 3. As expected, applying these FP parameters in our FAS-NMG framework with the MG parameters, the pre-smoothing step  $\nu_1 = 7$  and the post-smoothing step  $\nu_2 = 7$ , leads to convergent MG methods for Method 5. Obviously, Tab. 3.3 shows that Method 5 with the GFP smoother is the fastest way in our tests for solving the discrete nonlinear system (2.15) and producing good restoration results.



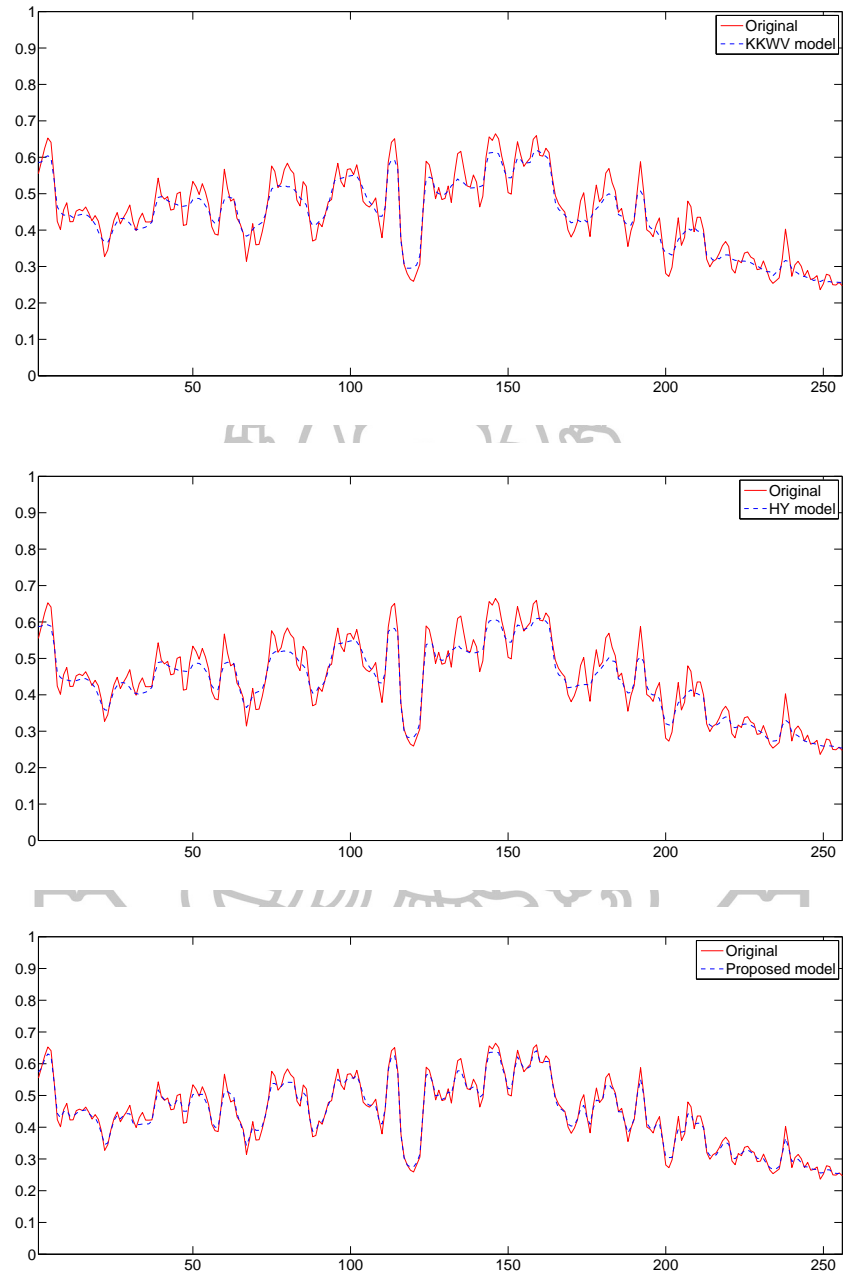


Figure 3.11: Corresponding signals of one column 128 of the liver image as shown in Fig. 3.8. Top row: recovered signal by KKWV model; middle row: recovered signal by HY model; bottom row: recovered by the proposed model.



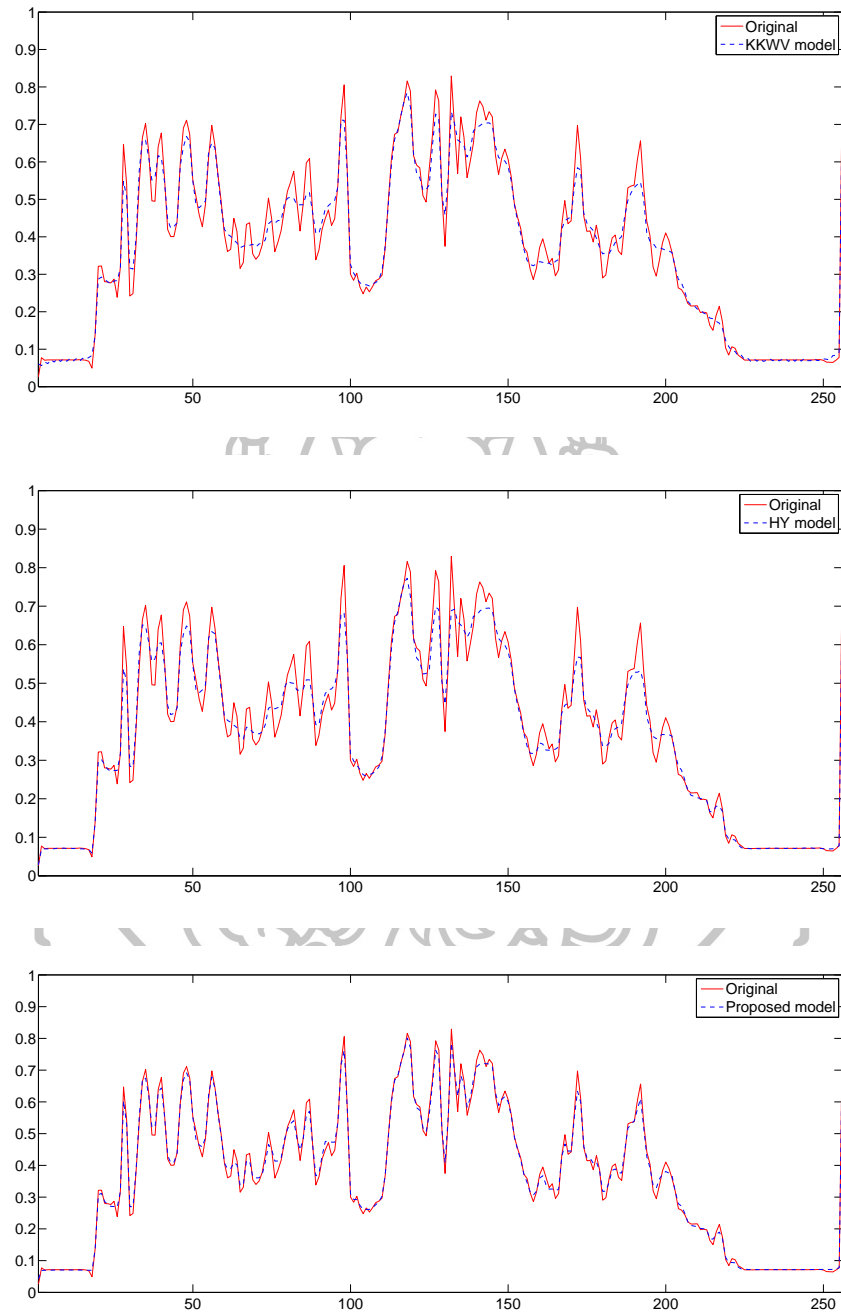


Figure 3.12: Corresponding signals of one column 128 of the kidney image as shown in Fig. 3.9. Top row: recovered signal by KKWV model; middle row: recovered signal by HY model; bottom row: recovered by the proposed model.

Image	Method 1		Method 2		Method 3		Method 4		Method 5	
	SFTM	AOS	GFP	LFP	CGLFP	GFP	LFP	CGLFP	GFP	LFP
<b>Ring</b>	N/CPU/s/PSNR	N/CPU/s/PSNR	N/CPU/s/PSNR	N/CPU/s/PSNR	N/CPU/s/PSNR	N/CPU/s/PSNR	N/CPU/s/PSNR	N/CPU/s/PSNR	N/CPU/s/PSNR	N/CPU/s/PSNR
$\alpha_1 = 10^{-4}$	11231.77/39.31	967.97/38.39	462/21.41/39.33	*/*/*	*/*/*	3/4.10/38.46	3/11.23/38.35	3/11.23/38.35	52/62/39.30	5/6.50/39.31
$\alpha_2 = 10^{-3}$										
$\epsilon = 10^{-2}$										
<b>Lena</b>										
$\alpha_1 = 10^{-4}$	33/9.24/29.00	41/3.78/25.96	48/2.19/29.05	99/9.29/29.13	182/15.43/29.24	3/3.96/28.90	3/10.46/28.53	3/8.74/27.86	3/1.37/28.96	3/3.29/29.00
$\alpha_2 = 5 \times 10^{-4}$										
$\epsilon = 10^{-2}$										
<b>Pepper</b>										
$\alpha_1 = 10^{-4}$	27/7.67/32.08	15/1.22/30.36	39/1.81/32.17	72/7.19/32.28	138/11.68/32.44	3/3.97/31.97	3/10.00/31.60	3/8.33/30.94	3/1.36/32.02	3/3.28/32.04
$\alpha_2 = 5 \times 10^{-4}$										
$\epsilon = 10^{-2}$										

Table 3.3: Performance tests among Methods 1–5 on the three test images shown in Fig. 3.1. The letters “N” and “CPU” means the number of iterations and the total run times (in seconds). \* indicates the computation was stopped after a failure in meeting Stop(1), Stop(2) or Stop(3).

### 3.4 Further performance tests on Method 5

In this section we present some results obtained from Method 5 or our proposed FAS-NMG method summarized in Algorithm 4 to show that its convergence properties are reliable with regard to parameter changes.

#### 3.4.1 $h$ -independent test

One of the key properties of MG techniques is that their convergence does not depend on the number of grid points.

As shown in Table 3.3, GFP smoother with the parameters  $\omega = 1.2$  and  $\max_{\text{SOR}} = 4$  is recommendable for our FAS-NMG framework in terms of fast convergence. Thus, in this test we designed our experiments to investigate the convergence property resulting from this GFP smoother. Here “N” represents the number of MG steps (cycles) used in Algorithm 4 with the stopping parameters  $\vec{\epsilon} = (20, 10^{-4}, 10^{-3}, 10^{-4})$ . The PSNR values and the run times are given in Table 3.4 with different sizes of grid points. Recall that  $\nu_1, \nu_2, \omega, \max_{\text{SOR}}$ , PSNR and CPUs denote the number of pre-smoothing and post-smoothing, the relaxation parameter, the maximum number of the inner iteration, the peak signal-to-noise ratio and the run times (in seconds), respectively.

As expected, the numerical results shown in Table 3.4 clearly confirm that the proposed FAS-NMG method is  $h$ -independent.

#### 3.4.2 Signal-dependent tests

Table 3.5 shows the robustness of our SN removal model and the proposed FAS-NMG method in Algorithm 4 for different noise levels.

Here we tested our proposed FAS-NMG method with the GFP smoother using the parameters  $h = 1/256$ ,  $\epsilon = 10^{-2}$ ,  $\nu_1 = \nu_2 = 7$ ,  $\omega = 1.2$ ,  $\max_{\text{SOR}} = 4$  and  $\vec{\epsilon} = (20, 10^{-4}, 10^{-3}, 10^{-4})$  for all tests on the image ring.

As can be clearly seen, although convergence is slower for noisier images, the PSNR

Image	MG with the GFP Smoother (Alg. 1)
	$\nu_1/\nu_2/N/PSNR/CPU_s$
<b>Ring</b>	$\alpha_1 = 10^{-4}, \alpha_2 = 10^{-3}, \epsilon = 10^{-2}$
$h = 1/128$	7/7/4/38.15/0.57
$h = 1/256$	7/7/5/39.03/2.62
$h = 1/512$	7/7/5/40.22/11.03
$h = 1/1024$	7/7/5/41.21/42.96
<b>Lena</b>	$\alpha_1 = 10^{-4}, \alpha_2 = 5 \times 10^{-4}, \epsilon = 10^{-2}$
$h = 1/128$	7/7/3/28.66/0.59
$h = 1/256$	7/7/3/28.96/1.37
$h = 1/512$	7/7/3/29.15/5.40
$h = 1/1024$	7/7/3/29.45/22.83
<b>Pepper</b>	$\alpha_1 = 10^{-4}, \alpha_2 = 5 \times 10^{-4}, \epsilon = 10^{-2}$
$h = 1/128$	7/7/3/30.63/0.42
$h = 1/256$	7/7/3/32.02/1.36
$h = 1/512$	7/7/3/32.26/5.43
$h = 1/1025$	7/7/3/32.46/21.92

Table 3.4: Restoration results of Algorithm 4 (Proposed FAS-NMG method) with the GFP smoother for the synthetic images in Fig.3.1 corrupted by SN with the standard deviation  $\sigma_n^2 = 10$ . Recall that  $\omega = 1.2$  and  $\max_{SOR} = 4$  were used in the GFP smoother.

and ReErr values show that the restored images would come with good quality. Moreover, the number of MG steps does not increase very much.

$\sigma_n^2$	1	5	10	15	20
N	3	4	5	5	5
PSNR	57.19	45.75	39.30	36.11	34.20
ReErr	$1.81 \times 10^{-5}$	$2.52 \times 10^{-4}$	$1.11 \times 10^{-3}$	$2.32 \times 10^{-3}$	$3.60 \times 10^{-3}$

Table 3.5: Restoration results for signal–dependent tests of Algorithm 4 (Proposed FAS-NMG method) with the GFP smoother for the image ring shown in Fig. 3.1. Note the regularization parameters for all tests were well-selected.

### 3.4.3 $\alpha_1/\alpha_2$ –dependent test

Next we evaluate to show how our FAS-NMG method in Algorithm 4 is affected with varying  $\bar{\alpha} = \alpha_1/\alpha_2$ .

To this end, the MG algorithm based on the GFP smoother was tested on the image ring (see Fig. 3.1) with the results shown in Table 3.6. Here the following parameters are used:  $\epsilon = 10^{-2}$ ,  $h = 1/256$ ,  $\nu_1 = \nu_2 = 7$ ,  $\omega = 1.2$ ,  $\max_{\text{SOR}} = 4$ ,  $\sigma_n^2 = 10$  and  $\vec{\epsilon} = (20, 10^{-4}, 10^{-3}, 10^{-4})$  for all experiments and  $\bar{\alpha}$  is varied from 0.01 to 100.

As can be seen from Table 3.6, decreasing the values of  $\alpha_2$  leads to the best restoration result at  $\bar{\alpha} = 0.2$ . Moreover, we can also see that large  $\bar{\alpha}$  is not needed as small ones give better results, typically  $\bar{\alpha} = 0.1, 0.2, 0.5, 1$ , and 2. We note that the process to select the optimal value of  $\bar{\alpha}$  is a separate but important issue because it is in general unknown a priori and it significantly affects on the qualities of restored images as well as the MG performance.

$\frac{\alpha_1}{\alpha_2}$	$\frac{10^{-4}}{10^{-2}}$	$\frac{10^{-4}}{10^{-3}}$	$\frac{10^{-4}}{0.5 \times 10^{-3}}$	$\frac{10^{-4}}{0.2 \times 10^{-3}}$	$\frac{10^{-4}}{10^{-4}}$	$\frac{10^{-4}}{0.5 \times 10^{-4}}$	$\frac{10^{-4}}{0.2 \times 10^{-4}}$	$\frac{10^{-4}}{10^{-5}}$	$\frac{10^{-4}}{10^{-6}}$
$\bar{\alpha}$	0.01	<b>0.1</b>	<b>0.2</b>	<b>0.5</b>	<b>1</b>	<b>2</b>	<b>5</b>	<b>10</b>	<b>100</b>
N	15	<b>5</b>	<b>4</b>	<b>4</b>	<b>3</b>	<b>3</b>	n.c.	n.c.	n.c.
PSNR	28.68	<b>39.30</b>	<b>40.22</b>	<b>34.98</b>	<b>31.38</b>	<b>29.69</b>	*	*	*
ReErr	$1.28 \times 10^{-2}$	$1.11 \times 10^{-3}$	$8.90 \times 10^{-4}$	$3.00 \times 10^{-3}$	$6.89 \times 10^{-3}$	$1.01 \times 10^{-2}$	*	*	*

Table 3.6: Restoration results for  $\alpha_1/\alpha_2$ -dependent tests of Algorithm 4 (Proposed FAS-NMG method) with the GFP smoother for the image ring shown in Fig. 3.1. Clearly, the small ratios between  $\alpha_1$  and  $\alpha_2$ , i.e.  $\bar{\alpha} = 0.1, 0.2, 0.5, 1$  and  $2$ , are recommended.

### 3.4.4 $\epsilon$ -dependent test

As is well known, the qualities of restoration results and the performance of the MG techniques in solving the nonlinear systems related to the TV regularization method are affected significantly by the values of  $\epsilon$ .

Here our aim for this test is to see how the proposed variational model and FAS-NMG algorithm are affected with varying the values of  $\epsilon$ . To see this, the MG algorithm based on the GFP smoother was tested on the image ring using the following parameters  $h = 1/256$ ,  $\alpha_1 = 10^{-4}$ ,  $\alpha_2 = 10^{-3}$ ,  $\sigma_n^2 = 10$ ,  $\nu_1 = \nu_2 = 7$ ,  $\omega = 1.2$ ,  $\max_{\text{SOR}} = 4$  and  $\vec{\epsilon} = (20, 10^{-4}, 10^{-3}, 10^{-4})$  for all experiments and  $\epsilon$  is varied from  $10^{-4}$  to  $5 \times 10^{-1}$ .

As can be seen, Table 3.7 shows that our FAS-NMG method with GFP smoother converges within a few MG steps for  $\epsilon \in [10^{-4}, 5 \times 10^{-1}]$ . Theoretically,  $\epsilon$  should be selected to be very small as much as possible. However our experimental results indicate

$\epsilon$	$5 \times 10^{-1}$	$2.5 \times 10^{-1}$	$10^{-1}$	<b><math>10^{-2}</math></b>	$10^{-3}$	$10^{-4}$
N	5	5	5	<b>5</b>	5	5
PSNR	38.08	38.40	38.75	<b>39.30</b>	39.51	39.57
ReErr	$1.47 \times 10^{-3}$	$1.37 \times 10^{-3}$	$1.26 \times 10^{-3}$	<b><math>1.11 \times 10^{-3}</math></b>	$1.05 \times 10^{-3}$	$1.04 \times 10^{-3}$

Table 3.7: Restoration results for  $\epsilon$ -dependent tests of Algorithm 4 (Proposed FAS-NMG method) with the GFP smoother for the image ring shown in Fig. 3.1. Clearly,  $\epsilon = 10^{-2}$  is enough to remove this kind of SN with the good PSNR results in a few MG steps.

that very small  $\epsilon$  is not necessary and not recommendable. As clearly shown in Table 3.4,  $\epsilon = 10^{-2}$  is enough to remove this kind of noise with the good PSNR and ReErr results. We note GFP smoother can lead to better MG convergence for the case  $\epsilon < 10^{-2}$  when the number of pre- and post-smoothing steps  $\nu_1$  and  $\nu_2$  are increased.



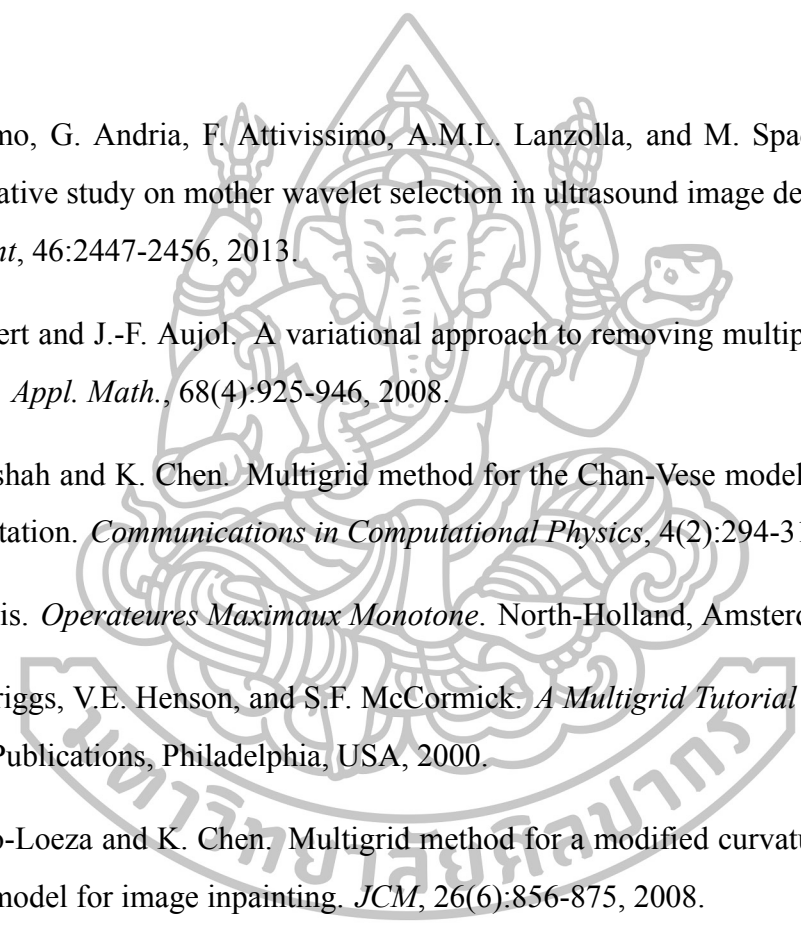
## Chapter 4

### Conclusion and future work

The main focus of author's work presented in this thesis is to study effective variational models and their efficient solution methods for removing SN from real US images. We have presented an improved variational model for removing SN from real US images based on the TV and WTV regularization methods. The existence and uniqueness of the solution for the improved variational model have also discussed. In order to solve the associated EL equation, we have proposed several numerical methods. Numerical tests confirmed that the model delivers better restoration results than the competing models and very importantly its MG solution is fast, robust and reliable in providing visually pleasing restoration results. There are still outstanding issues with our proposed model and algorithms; among others optimal selection of  $\alpha_1$  and  $\alpha_2$  is to be addressed. Future work will also consider generalization of this work to other image processing problems.



## References

- 
- [1] F. Adamo, G. Andria, F. Attivissimo, A.M.L. Lanzolla, and M. Spadavecchia. A comparative study on mother wavelet selection in ultrasound image denoising. *Measurement*, 46:2447-2456, 2013.
- [2] G. Aubert and J.-F. Aujol. A variational approach to removing multiplicative noise. *SIAM J. Appl. Math.*, 68(4):925-946, 2008.
- [3] N. Badshah and K. Chen. Multigrid method for the Chan-Vese model in variational segmentation. *Communications in Computational Physics*, 4(2):294-316, 2008.
- [4] H. Brezis. *Operateurs Maximaux Monotone*. North-Holland, Amsterdam, 1993.
- [5] W.L. Briggs, V.E. Henson, and S.F. McCormick. *A Multigrid Tutorial (2nd Edition)*. SIAM Publications, Philadelphia, USA, 2000.
- [6] C. Brito-Loeza and K. Chen. Multigrid method for a modified curvature driven diffusion model for image inpainting. *JCM*, 26(6):856-875, 2008.
- [7] C. Brito-Loeza and K. Chen. Fast numerical algorithms for Euler's Elastica digital inpainting model. *International Journal of Modern Mathematics*, 5(2):157-182, 2010.
- [8] C. Brito-Loeza and K. Chen. Multigrid algorithm for high order denoising. *SIAM J. Imaging Sci.*, 3(3):363-389, 2010.
- [9] C. Brito-Loeza and K. Chen. On high-order denoising models and fast algorithms for vector-valued images. *IEEE Trans. Image Process.*, 19(6):1518-1527, 2010.

- [10] T.F. Chan and K. Chen. On a nonlinear multigrid algorithm with primal relaxation for the image total variation minimization. *Journal of Numerical Algorithms*, 41:387-411, 2006.
- [11] T.F. Chan and K. Chen. An optimization-based multilevel algorithm for total variation image denoising. *Multiscale Mod. Simu.*, 5(2):615-645, 2006.
- [12] T.F. Chan, K. Chen, and X.-C. Tai. *Nonlinear multilevel scheme for solving the total variation image minimization problem*. in Proceedings of the International Conference on PDE-Based Image Processing and Related Inverse Problems Series: Mathematics and Visualization, edited by X.-C. Tai, K.-A. Lie, T.F. Chan and S. Osher, Springer Verlag, pp. 1-27, 2006.
- [13] T.F. Chan and P. Mulet. On the convergence of the lagged diffusivity fixed point method in total variation image restoration. *SIAM J. Numer. Analysis*, 36(2):354-367, 2007.
- [14] K. Chen and X.-C. Tai. A nonlinear multigrid method for total variation minimization from image restoration. *Journal of Scientific Computing*, 32(2):115-138, 2007.
- [15] Q. Chen, P. Montesinos, Q.S. Sun, and D.S. Xia. Ramp preserving Perona-Malik model. *Signal Processing*, 90:1963-1975, 2010.
- [16] N. Chumchob. Vectorial total variation-based regularization for variational image registration. *IEEE Trans. Image Process.*, 22(11):4551-4559, 2013.
- [17] N. Chumchob and K. Chen. A variational approach for discontinuity-preserving image registration. *East-West Journal of Mathematics*, Special volume 2010:266-282, 2010.
- [18] N. Chumchob and K. Chen. A robust multigrid approach for variational image registration models. *Journal of Computational and Applied Mathematics*, 236:653-674, 2011.

- [19] N. Chumchob and K. Chen. An improved variational image registration model and a fast algorithm for its numerical approximation. *Numerical Methods for Partial Differential Equations*, 28(6):1966-1995, 2012.
- [20] N. Chumchob, K. Chen, and C. Brito. A fourth order variational image registration model and its fast multigrid algorithm. *SIAM J. Multiscale Modeling and Simulation*, 9:89-128, 2011.
- [21] N. Chumchob, K. Chen, and C. Brito. A new variational model for removal of combined additive and multiplicative noise and a fast algorithm for its numerical approximation. *International Journal of Computer Mathematics*, 90(1):140-161, 2013.
- [22] V. Dutt and J. Greenleaf. Adaptive speckle reduction filter for log-compressed B-scan images. *IEEE Trans. Med. Imag.*, 15(6):802-813, 1996.
- [23] C. F.-Schauf, S.Henn, and K. Witsch. Nonlinear multigrid methods for total variation image denoising. *Comput. Visual. Sci.*, 7:199-206, 2004.
- [24] S. Geman and D. Geman. Stochastic relaxation, gibbs distributions, and the bayesian restoration of images. *IEEE Trans. Pattern Anal. Mach Intel.*, 6(6):721-741, 1984.
- [25] E. Giusti. *Minimal Surfaces and Functions of Bounded Variation. Monographs in Mathematics, Vol. 80.* Birkhauser, Boston, 1984.
- [26] E. Haber and J. Modersitzki. A multilevel method for image registration. *SIAM J. Sci. Comput.*, 27(5):1594-1607, 2006.
- [27] X.H. Hao, S.K. Gao, and X.R. Gao. A novel multiscale nonlinear thresholding method for ultrasonic speckle suppressing. *IEEE Trans. Med. Imaging.*, 18(9):787-794, 1999.
- [28] P. Hellier, C. Kervrann, and C. Barillot. Nonlocal means-based speckle filtering for ultrasound images. *IEEE Trans. Image Process.*, 18(10):2221-2229, 2009.

- [29] L.-L. Huang, L. Xiao, and Z.-H. Wei. Multiplicative noise removal via a novel variational model. *EURASIP Journal on Image and Video Processing*, 250768:DOI: 10.1155/2010/25076, 2010.
- [30] Y. Huang, M. Ng, and Y. Wen. A new total variation method for multiplicative noise removal. *SIAM J. Imaging Sci.*, 2(1):20-40, 2009.
- [31] J.B.-Dias and M.A.T. Figueiredo. Multiplicative noise removal using variable splitting and constrained optimization. *IEEE Trans. Image Process.*, 19(7):1720-1730, 2010.
- [32] J.Huang and X.Yang. Fast reduction of speckle noise in real ultrasound images. *Signal Processing*, 93:684-694, 2013.
- [33] Z. Jin and X. Yang. Analysis of a new variational model for multiplicative noise removal. *J. Math. Anal. Appl.*, 362:415-426, 2010.
- [34] Z. Jin and X. Yang. A variational model to remove the multiplicative noise in ultrasound images. *J. Math Imaging Vis*, 39:62-74, 2011.
- [35] J.Shen. On the foundations of vision modeling: I. Weber's law and Weberized TV restoration. *Physica D: Nonlinear Phenomena*, 175(3-4):241-251, 2003.
- [36] J. Koo and S.B. Oark. Speckle reduction with edge preservation in medical ultrasonic images using a homogenous region growing mean filter (HRGMF). *Ultrasonic Imaging*, 13:629-639, 1990.
- [37] J. Koo and S.B. Oark. Despeckling of medical ultrasound images using daubechies complex wavelet transform. *Signal Processing*, 90:428-439, 2010.
- [38] P. Kornprobst, R. Deriche, and G. Aubert. Image sequence analysis via partial differential equations. *J. Math. Imaging Vis.*, 11(1):5-26, 1999.
- [39] K. Krissian, R. Kikinis, C.F. Westin, and K. K. Vosburgh. Speckle constrained filtering of ultrasound images. *IEEE Comput. Vis. Pattern Recogn.*, 15:547-552, 2005.

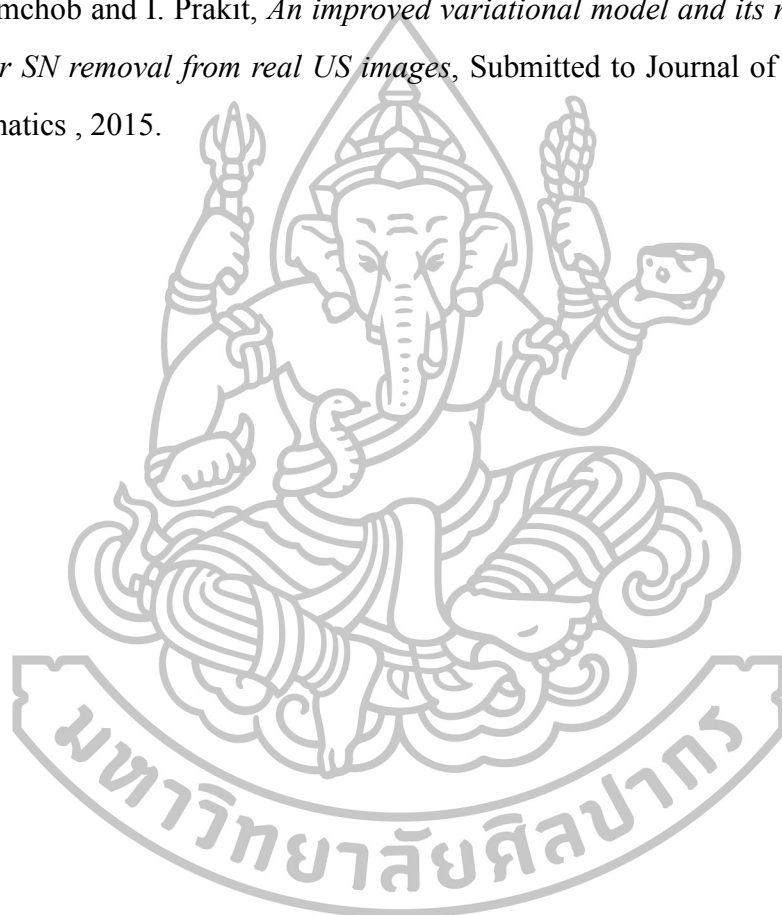
- [40] T. Loupas, W. McDicken, and P. Allan. An adaptive weighted median filter for speckle suppression in medical ultrasound images. *IEEE Transactions on Circuits and Systems*, 36(1):129-135, 1989.
- [41] O.V. Michailovich and A. Tannenbaum. An accurate and efficient bayesian model for automatic segmetation of brain MRI. *IEEE Trans. Ultrason., Ferroelect., Freq. Contr.*, 53(1):64-78, 2006.
- [42] S. Osher, M. Burger, D. Goldfarb, J. Xu, and W.T. Yin. An iterative regularization method for total variation-based image restoration. *Multiscale Mod. Simu.*, 4:460-489, 2005.
- [43] W.C. Rheinboldt. *Methods for Solving Systems of Nonlinear Equations (2nd Edition)*. SIAM Publications, Philadelphia, USA, 1998.
- [44] L. Rudin, S. Osher, and E. Fatemi. Nonlinear total variation based noise removal algorithms. *Physica D*, 60:259-268, 1992.
- [45] L. I. Rudin, P. L. Lions, and S. Osher. *Multiplicative denoising and deblurring: theory and algorithms*, in *Geometric Level Set Methods in Imaging, Vision, and Graphics*, S. Osher and N. Paragios, Eds., pp. 103-120. Springer, Berlin, Germany, 2003.
- [46] Y. Saad. *Iterative Methods for Sparse Linear Systems (2nd Edition)*. SIAM Publications, Philadelphia, USA, 2003.
- [47] J. Savage and K. Chen. An improved and accelerated nonlinear multigrid method for total-variation denoising. *International Journal of Computer Mathematics*, 82(8): 1001-1015, 2005.
- [48] J. Savage and K. Chen. *On multigrids for solving a class of improved total variation based staircasing reduction models*. in Proceedings of the International Conference on PDE-Based Image Processing and Related Inverse Problems Series: Mathematics

and Visualization, edited by X.-C. Tai, K.-A. Lie, T.F. Chan and S. Osher, Springer Verlag, pp. 69-94, 2006.

- [49] J.N. Shi and S. Osher. A nonlinear inverse scale space method for a convex multiplicative noise model. *SIAM J. Imaging Sci.*, 1(3):294-321, 2008.
- [50] J.M. Thijssen. Ultrasonic speckle formation, analysis and processing applied to tissue characterization. *Pattern Recognition Letters*, 24:659-675, 2003.
- [51] U. Trottenberg, C. Oosterlee, and A. Schuller. *Multigrid*. Academic Press, 2001.
- [52] T.A. Tuthill, R.H. Sperry, and K.J. Parker. Derivation from rayleigh statistics in ultrasonic speckle. *Ultrason. Imag.*, 10:81-90, 1988.
- [53] C.R. Vogel. *A mutigrid method for total variation-based image denoising*. Computation and control IV, 20, Progress in systems and control theory, Birkhauser, 1995.
- [54] C.R. Vogel and M.E. Oman. Iterative methods for total variation denoising. *SIAM J. Sci. Comput.*, 17(1):227-238, 1996.
- [55] J. Weickert, B.M. ter Haar Romeny, and M. Viergever. Efficient and reliable schemes for nonlinear diffusion filtering. *IEEE Trans. Image Process.*, 7:398-410, 1998.
- [56] R. Wienands and W. Joppich. *Practical Fourier Analysis for Multigrid Method*. Chapman & Hall/CRC, U.S.A., 2005.
- [57] H. Yua, J.L.Tana, and Y.Y.Wang. Ultrasound speckle reduction by a SUSAN-controlled anisotropic diffusion method. *Pattern Recognition*, 43:3083-3092, 2010.

### Publications

- I. Prakit and N. Chumchob, *A Multi-Resolution Method for Removing the Multiplicative Noise in Medical Ultrasound Images*, The Proceeding of 53rd Kasetsart University Annual Conference, February 3-6, 2015, pp. 10-17.
- N. Chumchob and I. Prakit, *An improved variational model and its numerical solutions for SN removal from real US images*, Submitted to Journal of Computational Mathematics , 2015.



## Biography

Name	Miss Isararat Prakit
Address	76 Moo 5 Tambol Nongbuaraway, Amphur Nongbuaraway, Chaiyaphum, 36250
Date of Birth	8 March 1990
Education	
2012	Bachelor of Science in Applied Mathematics, Silpakorn University
2015	Master of Science in Mathematics, Silpakorn University

